

**INSTALLATION AND OPERATION OF PARTICLE TRANSPORT
SIMULATION PROGRAMS TO MODEL THE DETECTION AND
MEASUREMENT OF SPACE RADIATION BY SPACE-BORNE
SENSORS**

Dr. Stanley Woolf

**Arcon Corporation
260 Bear Hill Road
Waltham, MA 02541-1080**

25 September 2003

Final Report

BEST AVAILABLE COPY

20040415 054

APPROVED FOR PUBLIC RELEASE; DISTRIBUTION UNLIMITED



**AIR FORCE RESEARCH LABORATORY
Space Vehicles Directorate
29 Randolph Rd
AIR FORCE MATERIEL COMMAND
Hanscom AFB, MA 01731-3010**

This technical report has been reviewed and is approved for publication.

/Signed/
BRONISLAW K. DICHTER
Contract Manager

/Signed/
ROBERT A. MORRIS
Branch Chief

This document has been reviewed by the ESC Public Affairs Office and has been approved for release to the National Technical Information Service.

Qualified requestors may obtain additional copies from the Defense Technical Information Center (DTIC). All others should apply to the National Technical Information Service.

If your address has changed, if you wish to be removed from the mailing list, or if the addressee is no longer employed by your organization, please notify AFRL/VSIM, 29 Randolph Rd., Hanscom AFB, MA 01731-3010. This will assist us in maintaining a current mailing list.

Do not return copies of this report unless contractual obligations or notices on a specific document require that it be returned.

REPORT DOCUMENTATION PAGE					Form Approved OMB No. 0704-0188	
<p>The public reporting burden for this collection of information is estimated to average 1 hour per response, including the time for reviewing instructions, searching existing data sources, gathering and maintaining the data needed, and completing and reviewing the collection of information. Send comments regarding this burden estimate or any other aspect of this collection of information, including suggestions for reducing the burden, to Department of Defense, Washington Headquarters Services, Directorate for Information Operations and Reports (0704-0188), 1215 Jefferson Davis Highway, Suite 1204, Arlington, VA 22202-4302. Respondents should be aware that notwithstanding any other provision of law, no person shall be subject to any penalty for failing to comply with a collection of information if it does not display a currently valid OMB control number.</p> <p>PLEASE DO NOT RETURN YOUR FORM TO THE ABOVE ADDRESS.</p>						
1. REPORT DATE (DD-MM-YYYY) 25-09-2003		2. REPORT TYPE Final Report		3. DATES COVERED (From - To) 10 August 1999 - 31 August 2003		
4. TITLE AND SUBTITLE Installation and Operation of Particle Transport Simulation Programs to Model the Detection and Measurement of Space Radiation by Space-borne Sensors				5a. CONTRACT NUMBER F19628-99-C-0077		
				5b. GRANT NUMBER		
				5c. PROGRAM ELEMENT NUMBER		
6. AUTHOR(S) Dr. Stanley Woolf				5d. PROJECT NUMBER 2822		
				5e. TASK NUMBER GC		
				5f. WORK UNIT NUMBER AR		
7. PERFORMING ORGANIZATION NAME(S) AND ADDRESS(ES) ARCON Corporation, 260 Bear Hill Rd., Waltham, MA 02451-1080				8. PERFORMING ORGANIZATION REPORT NUMBER		
9. SPONSORING/MONITORING AGENCY NAME(S) AND ADDRESS(ES) Air Force Research Laboratory (AFRL) 29 Randolph Road Hanscom AFB, MA 01731-3010 Contract Manager: Dr. Bronislaw K. Dichter / VSBXR				10. SPONSOR/MONITOR'S ACRONYM(S)		
				11. SPONSOR/MONITOR'S REPORT NUMBER(S) AFRL-VS-HA-TR-2004-1005		
12. DISTRIBUTION/AVAILABILITY STATEMENT Approved for public release, distribution unlimited						
13. SUPPLEMENTARY NOTES						
14. ABSTRACT <p>This document is a report of the work performed during the period 10 Aug. 1999 - 31 Aug. 2003 in the areas of: (1) research, evaluation and adaptation of particle transport simulation programs for modeling the detection and measurement of space radiation by space-borne sensors; (2) the transfer of this particle transport simulation capability to the Air Force Research Laboratory, Space Weather Center of Excellence (AFRL/VSBXR); (3) construction of realistic flight sensor computer models; (4) performance of particle transport calculations; (5) space-borne dosimeter simulation studies; and (6) studies of scattering of grazing incidence protons from surfaces of material constituents of space-borne X-ray telescopes. The computer programs ITS-ACCEPT and MCNPX were applied to the modeling of the CEASE and HEP sensors, and the CRRES dosimeter. This document also summarizes our collaboration in research leading to the publication of two technical papers.</p>						
15. SUBJECT TERMS <p>Electron and proton transport; Monte Carlo simulation; Space-borne sensor modeling; ITS/ACCEPT Code; MCNPX Code; Dosimeters; grazing angle proton scatter; CEASE; CRRES; PASP; Chandra X-ray Telescope</p>						
16. SECURITY CLASSIFICATION OF:			17. LIMITATION OF ABSTRACT SAR	18. NUMBER OF PAGES 45	19a. NAME OF RESPONSIBLE PERSON Dr. Bronislaw Dichter	
a. REPORT Unclassified	b. ABSTRACT Unclassified	c. THIS PAGE Unclassified			19b. TELEPHONE NUMBER (Include area code) (781)377-3991	

Contents

	Page
1. Introduction	1
2. Electron Transport Modeling	2
2.1 Electron Transport Modeling for the CEASE Telescope	
2.1.1 CYLTRAN Simulation for the CEASE Telescope	2
2.2 Electron Energy Deposition Calculations in Silicon Wafers	3
2.3 ITS-ACCEPT Electron/Photon Transport Simulations for the HEP Instrument	7
2.4 ITS-ACCEPT Program Enhancements	8
2.4.1 Disk and Rectangle Source Options	8
2.4.2 Individual Electron Track Option	8
2.5 Dome Dosimeter Studies	10
2.6 CEASE Dosimeter Models	12
2.7 PASP Dosimeter Models	13
2.8 CRRES Dosimeter Modeling	15
3. Proton Transport Modeling	15
3.1 HEP Flight Sensor Simulations of Proton Transport With MCNPX	15
3.2 Simulations of Proton Transport in the CEASE Telescope With MCNPX	18
3.3 Grazing Angle Proton Scattering Calculations	19
4. Summary	21
References	23
Appendix A	26
Appendix B	35

Figures

	Page
1. Total Energy Deposition [MeV] in Si Wafer ($0.05 \times 0.9 \times 0.9 \text{ cm}^3$) for 8 Source Geometries; Electron Energy = 6 MeV	5
2. Energy Deposition [MeV] in 5 Z-layers in Si Wafer ($0.05 \times 0.9 \times 0.9 \text{ cm}^3$), 6 MeV Electron Isotropic 45 deg. Cone Sources, Uniformly Distributed on Disk ($R=0.02 \text{ cm}$) centered at (0.025, 0.45, 0.0); ITS-ACCEPT calculation.	6
3. Sabrina rendering of ITS-ACCEPT Geometry Model of HEP Flight Sensor	7
4. Aluminum / Void / Silicon ACCEPT Problem Geometry (not drawn to scale) With Slant Disk Source As Described in the Input Data File Shown in 5.	9
5. ACCEPT Input Data File for 3.5 MeV 45° Slant Disk Source Incident on Aluminum / Void / Silicon Configuration Shown in 4.	10
6. CEASE DD1 and DD2 Dosimeter Assemblies.	11
7. CEASE DD1 and DD2 Dosimeter Geometry Schematic for ACCEPT Showing Plane Isotropic Electron Source.	11
8. CEASE DD1 and DD2 Dosimeter Geometry Schematic for ACCEPT Showing Hemispherically Shaped Isotropic Electron Source.	12
9. CEASE DD1 and DD2 Dosimeter Geometry Schematic for MCNPX Showing Hemispherically Shaped Isotropic Electron Source.	13
10. PASP Dome 2 Dosimeter Geometry Schematic for ACCEPT Showing Isotropic Electron Source Incident on Surface of Al Dome.	14
11. PASP Dome 2 Dosimeter Geometry Schematic for MCNPX Showing Isotropic Electron or Proton Source Incident on Surface of Al Dome.	14
12. Comparison of Flux and Dose Response Functions Calculated With ITS-ACCEPT and As Reported by Auchampaugh and Cayton.	16
13. Energy Depositions Due to Protons in DBT vs. DFT for the CEASE Telescope As Computed With the MCNPX Simulation Program	18
14. Computed Energy Depositions Due to Protons in DBT vs. DFT for the CEASE Telescope [<i>Brautigam, 2000</i>]	18
15. Sample Plots of Probability Density $P_{\theta} \left(\frac{(\theta_{out} - 90^\circ)}{(\theta_{in} - 90^\circ)}; E_{out} \right)$ of Emergent Protons from Iridium With Exit Polar Angle θ_{out} , for Incident Angle $\theta_{in} = 90.5^\circ$, for Source Energy $E_{in} = 250 \text{ keV}$ and Exit Energy Bins $E_{out} = 0\text{-}12.5, 12.5\text{-}25.0, 25.0\text{-}37.5, 37.5\text{-}50.0, 50.0\text{-}62.5 \text{ keV}$	20

Tables

	Page
1. Eight Source Configurations for Transport Simulation of 4.0 and 6.0 MeV Electrons in Silicon	4
2. Comparison of ITS/ACCEPT and MCNPX Energy Deposition (MeV) Calculations for CRRES_D1 Dosimeter (ALL CELLS, Figures 1,3) for Four Source Energies	17

1. INTRODUCTION

ARCON Corporation is pleased to submit the following Final Report, which describes the research and modeling effort that has been carried out under the provisions of contract # F19628-99-C-0077. There are sections summarizing the work we did on: (1) electron transport modeling; (2) CEASE[Dichter *et al.*, 1998] and Photovoltaic Array and Space Power (PASP) [Gussenhoven *et al.*, 1995, 1997] Dome dosimeter modeling; (3) ionizing particle energy deposition and coincidence event identification in the Compact Environmental Anomaly Sensor (CEASE); (4) ionizing particle energy deposition in the High Energy Particle (HEP) instrument [Redus, 1998]; (5) proton transport modeling; and (6) simulation studies of grazing angle proton scattering.

The overall objectives of the work that we have undertaken are to: (1) perform computer simulations of charged particle transport, energy and charge deposition in satellite-borne instrumentation used in research efforts of the Air Force Research Laboratory, Space Weather Center of Excellence (AFRL/VSBXR) to detect and characterize (by type, energy, intensity, *etc.*) particles associated with ionizing radiation in space; (2) transfer this simulation capability to AFRL/VSBXR and provide advice to Air Force researchers on its use; (3) participate in the AFRL research effort by providing the particle transport simulation component of the research; and (4) enhance the capabilities of existing Monte Carlo transport programs by modifying these programs to satisfy specific requirements of the AFRL research effort. We believe that these stated goals are well served by the work reported below.

Our report is accompanied by two papers, a reprint and a pre-print, in which the author of this report participated as co-author, that were published in *IEEE Transactions on Nuclear Science* during the performance period of this contract, which was from 10 August 1999 until 31 August 2003. The first of these [Brautigam *et al.*, 2001] deals with the solar cycle variation of outer belt electron dose at low-earth orbit. Our participation in this research effort consisted of a Monte Carlo analysis of the relative response of the CEASE and PASP dosimeters that were used to perform the electron dose measurements. This paper is included as Appendix A. The other paper deals with an investigation into the causes of the proton damage to one of the Chandra X-Ray telescope focal plane detectors. This paper demonstrates how use of standard proton transport Monte Carlo calculations of grazing angle proton scattering produces significant under prediction of the proton flux at the telescope focal plane. This paper [Dichter and Woolf, 2003] comprises Appendix B.

2. ELECTRON TRANSPORT MODELING

The modeling of electron transport, energy and charge deposition was accomplished using two Monte Carlo codes, the ITS 3.0 Code System [Halbleib *et al.*, 1992] and the multi-particle transport code MCNPX [Waters, 1999]. The first of these, ITS (Integrated TIGER Series of Coupled Electron/Photon Monte Carlo Codes) incorporates detailed physical models for electron and photon scattering and transport, secondary electron production, bremsstrahlung production, straggling and knock-on electron production. The second code, MCNPX, incorporates all the advantages of the Los Alamos MCNP code system [Briesmeister, 1997], such as problem geometry specification and code documentation, while possessing the capability of transporting 34 particle types (including antiparticles). This code was acquired primarily for the purpose of simulating proton transport, but also proved to be an effective tool for electrons.

2.1 Electron Transport Simulations for the CEASE Telescope

Electron transport calculations were made with the ITS-ACCEPT code for the CEASE Telescope. The ACCEPT code geometry modeling technique is based on the combinatorial geometry method in which the geometry model is constructed using a combination of body shapes offered by a collection of basic body types: arbitrarily oriented box(BOX); rectangular parallelepiped(RPP); sphere(SPH); right circular(RCC) and elliptical cylinders(REC); ellipsoid(ELL); truncated cone(TRC); wedge(WED); arbitrary polyhedron(ARB). For the CEASE telescope without the frame and case, a total of 205 bodies and 205 cells were defined. The addition of the frame and case to the telescope description increased the total numbers of bodies and cells to 259. A typical input file [Woolf, 2000] sets up a 25000 case history ACCEPT run for a 9.9 MeV electron beam normally incident on the top of the aluminum case. The beam cross sectional area is a disk of radius 1.4 cm with its center located on the CEASE axis of symmetry.

Two sets of ACCEPT runs were made for the CEASE telescope: telescope without and with the frame and case. For each configuration, the runs were made for two beam energies, 9.9 and 6.0 MeV, with three incident obliquities. The details of these runs and a summary of the results obtained are reported in Woolf [2000]. The purpose of this investigation was to obtain an estimate of the extent to which the structure surrounding the telescope would affect the resulting energy and charge deposition within the telescope.

Another geometry model of the CEASE Telescope was also made for use with MCNPX, and some electron transport calculations were made paralleling those discussed above. The ITS-ACCEPT and MCNPX geometry models were equivalent with respect to every detail.

2.1.1 CYLTRAN Simulation for the CEASE Telescope

The CYLTRAN [Halbleib *et al.*, 1992] Monte Carlo code is the 2-dimensional cylindrical geometry component of the ITS code series. It is applicable only in situations where the problem geometry can be approximated assuming total cylindrical symmetry. This symmetry condition was not strictly true for the CEASE telescope, however considerable economy of computational effort was achieved because the CYLTRAN code which requires far less computer time than ACCEPT if the problem geometry can

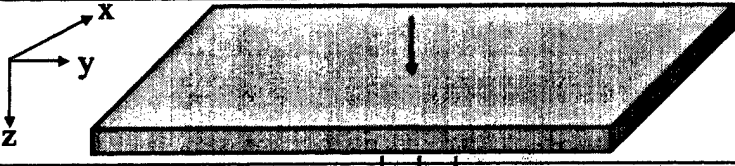
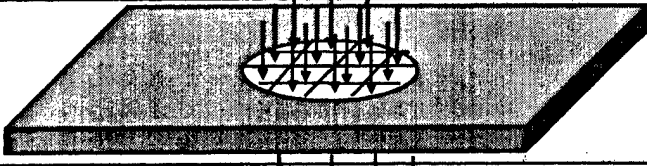
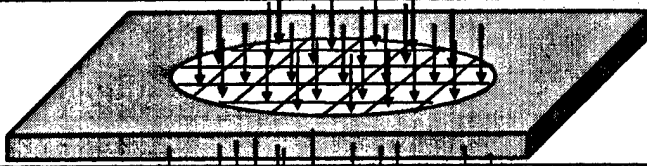

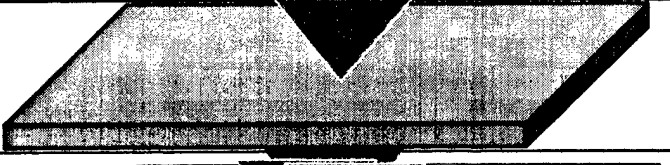

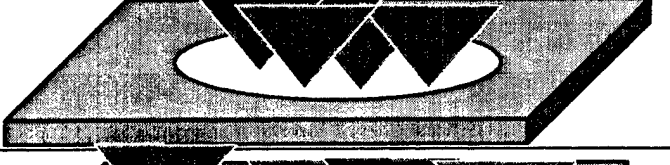
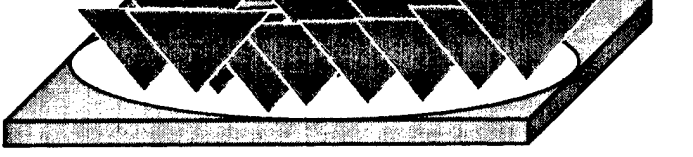
be adequately approximated in this context. Nearly equivalent results, reported in Woolf [2000] were obtained with both codes.

2.2 Electron Energy Deposition Calculations in Silicon Wafers

Transport calculations were made for 4 MeV and 6 MeV electrons incident on rectangular silicon dosimeter wafers ($0.05\text{cm} \times 0.9\text{cm} \times 0.9\text{cm}$). The Monte Carlo runs were made using 200,000 case histories for all source configurations and both source energies. The sources, all located on the wafer surfaces, consisted of: normally incident electron beams (or point sources); point isotropic sources; disk sources-normal incidence; disk sources-isotropic incidence. The source configurations are illustrated in Table 1. Default values for the electron low energy cut-off were used with both ACCEPT ($0.05E_{\text{source}}$) and MCNPX (1.0 keV). The default value for the MCNPX cut-off energy was set much lower than the ACCEPT value, resulting in run times for MCNPX (~1 hr) exceeding those for ACCEPT (~0.5 min). When the same electron cut-off energy was used in MCNPX, the run time was found to be a factor of 1.5 greater than that required for ACCEPT.

Duplicate simulation runs were made with both ITS-ACCEPT and MCNPX. Two objectives were accomplished with these calculations: (1) a set of input files was provided for both simulation programs that could be modified and used by AFRL personnel; and (2) the relative advantages and disadvantages of the ACCEPT and MCNPX codes for electron transport were compared. The input files were also configured to produce electron pulse-height spectra outputs. We provided interpretation of the pulse-height spectra results for both codes. Sample energy deposition results obtained with ACCEPT for the 6 MeV sources are shown in Figures 1 and 2.

Table 1.
Eight Source Configurations for Transport Simulation of 4.0 and 6.0 MeV Electrons in Silicon
[Woolf, 2002]

Electron Source Configuration	Source Geometry
(1) Single Beam, Normal Incidence at (.45,.45,0.)	
(2) Disk Source, Rad. = 0.1cm, Normal Incidence centered at (.45,.45,0.)	
(3) Disk Source, Radius = 0.2cm, Normal Incidence centered at (.45,.45,0.)	
(4) Disk Source, Radius = 0.449cm, Normal Incidence centered at (.45,.45,0.)	
(5) Point Isotropic, 45° cone centered at (.45,.45,0.)	
(6) Disk Source, Rad. = 0.1cm, Isotropic 45° cones centered at (.45,.45,0.)	
(7) Disk Source, Rad. = 0.2cm, Isotropic 45° cones centered at (.45,.45,0.)	
(8) Disk Source, Rad. = 0.449cm, Isotropic 45° cones centered at (.45,.45,0.)	

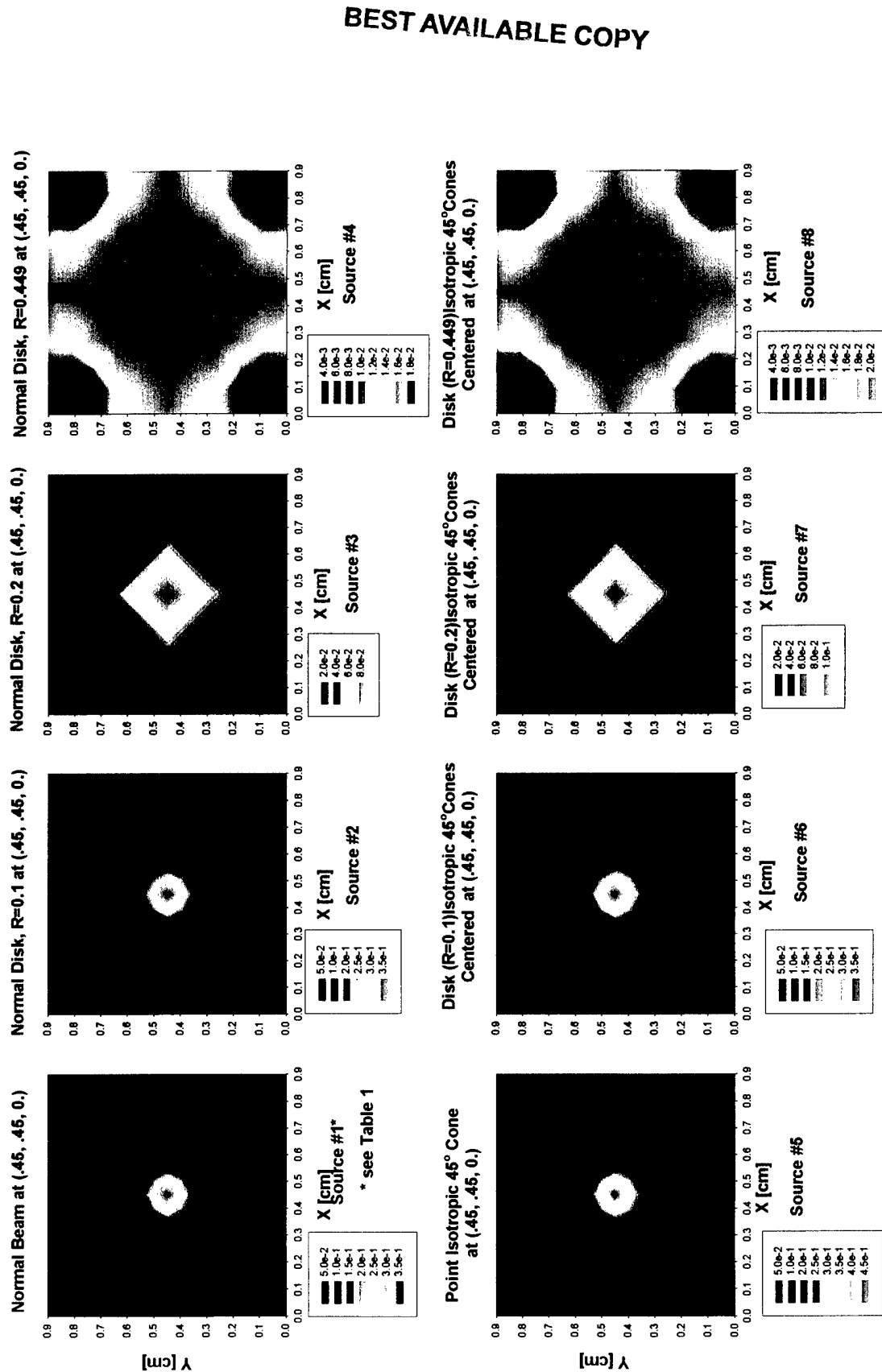
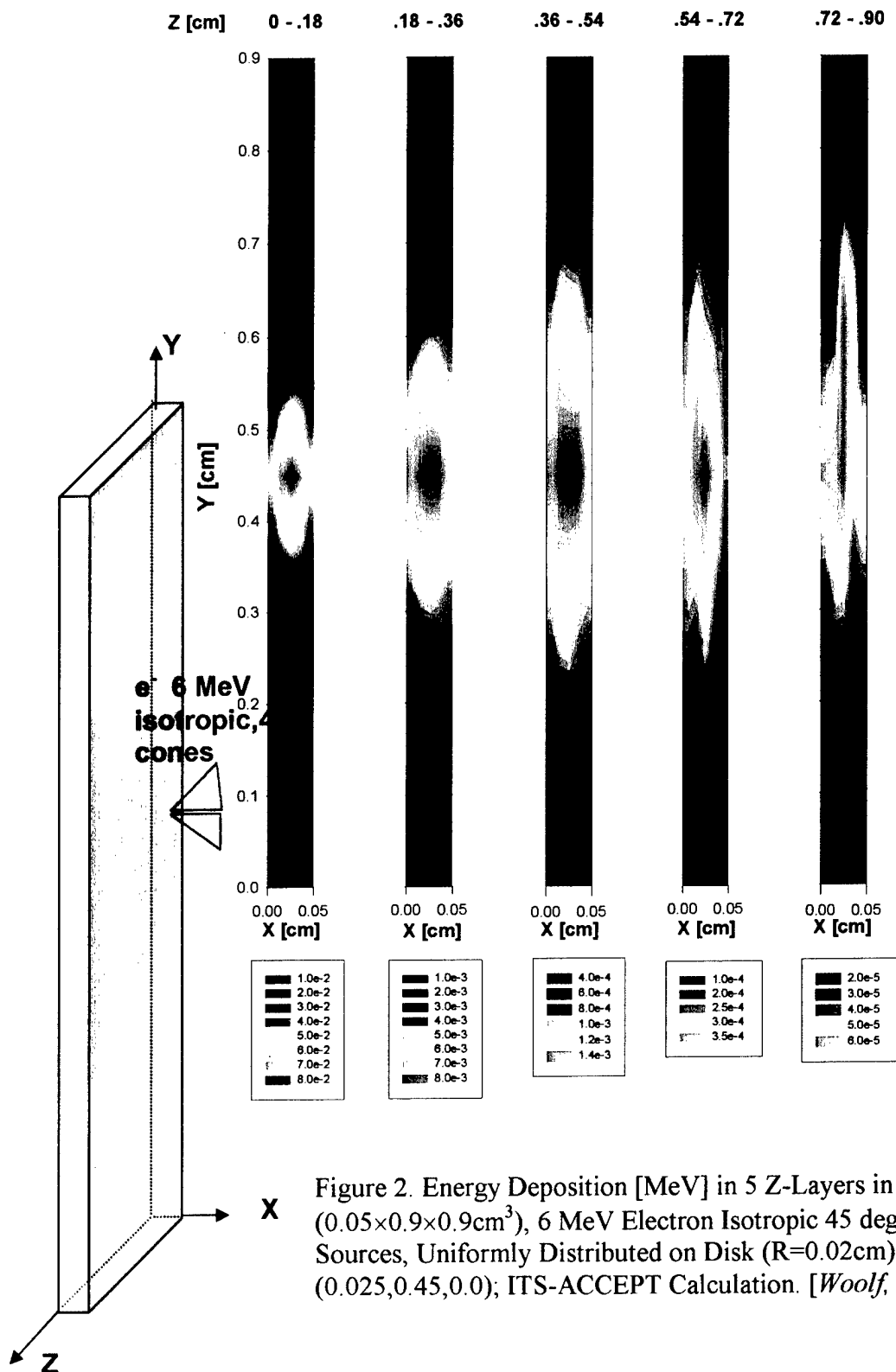


Figure 1. Total Energy Deposition [MeV] in Si Wafer (0.05x0.9x0.9cm³) for 8 Source Geometries; Electron Energy = 6 MeV [Woolf, 2002].



2.3 ITS-ACCEPT Electron/Photon Transport Simulations for the HEP Instrument

An ACCEPT geometry input file for the HEP instrument was created from the manufacturing drawings supplied by Amptek, Inc. [Redus, 1998]. The ACCEPT geometry description contains the same degree of detail as the manufacturing drawings permitted: (1) taking advantage of the speed and efficiency of the ACCEPT code for performing coupled electron-photon transport calculations in complicated structures; and (2) use of the ACCEPT code to confirm the validity of the MCNPX geometry description by comparing electron transport results obtained with the two programs. Unlike ACCEPT, MCNPX could also be used to perform transport calculations for protons, neutrons, mesons, and other particle species. It was therefore important to have the ACCEPT version of the HEP geometry to use as an independent verification of the MCNPX geometry description. The ACCEPT input file listing can be found in Woolf, 2002, Appendix 1. Several ACCEPT runs were made to test the robustness of this geometry file. The purpose was to uncover "holes" (errors) in the geometry specification due to improper cell definition. Test runs of ACCEPT were made with the model development at graduated stages of complexity until the full model illustrated in the SABRINA [Van Riper, 2001] visualization shown in Figure 3 passed all tests for robustness.



Figure 3. Sabrina [Van Riper, 2001] Rendering of ITS-ACCEPT Geometry Model of HEP Flight Sensor.

BEST AVAILABLE COPY

2.4 ITS-ACCEPT Program Enhancements

Modifications to the ITS-ACCEPT Monte Carlo program were made to provide the code with additional capabilities that would be useful in the design and evaluation of AFRL space-borne radiation sensors. These modifications fall into two categories: the addition of new source options; and the addition of code that permits the user to view the energy deposition contributions of individual electron tracks. The primary motivation for the source option enhancement was supplied by the fact that the standard disk source option in ACCEPT does not allow for the specification of electron source beam slant angles without slanting the source plane. Source electrons emanating from a plane with off-normal angles of incidence could not originate at equidistant points from the target. The demonstration of this is given in a set of electron transport runs that were made for the aluminum-void-silicon slab geometry shown in Figure 4. Runs with 3.5 MeV electron sources were made for six source disk slant angles. An ACCEPT input data file corresponding with $\theta = 45^\circ$, with the radius R of the disk source set at 1.0 cm., is shown in Figure 5.

2.4.1 Disk and Rectangle Source Options

Code additions were written and installed into the ACCEPT program to allow for disk and rectangular spatially uniform distributed sources (electrons or photons). This permits the user to change the slant angle of the source beam direction without slanting the source plane itself. The form of the input lines required to activate these options are given in Section 2.3.1 of Woolf, 2002. The code that was added to ACCEPT also prints diagnostic messages in the standard ITS format and aborts the run if an error in the input data violates the conditions for geometric validity.

Validation runs were made for both the rectangle and disk source cases.

2.4.2 Individual Electron Track Option

Another modification made to the ACCEPT program permits the user to view the energy deposition contributions of individual case histories (electron tracks) in as many as 10 problem geometry cells. The form of the input line for implementation of this option and sample outputs are given in Section 2.3.2 of Woolf, 2002.

The program listings containing these modifications to ACCEPT that incorporate the "RECTANGLE - SOURCE", "CIRCLE - SOURCE" and "INDIVIDUAL - HISTS" options are given in Appendix 2 of Woolf, 2002.

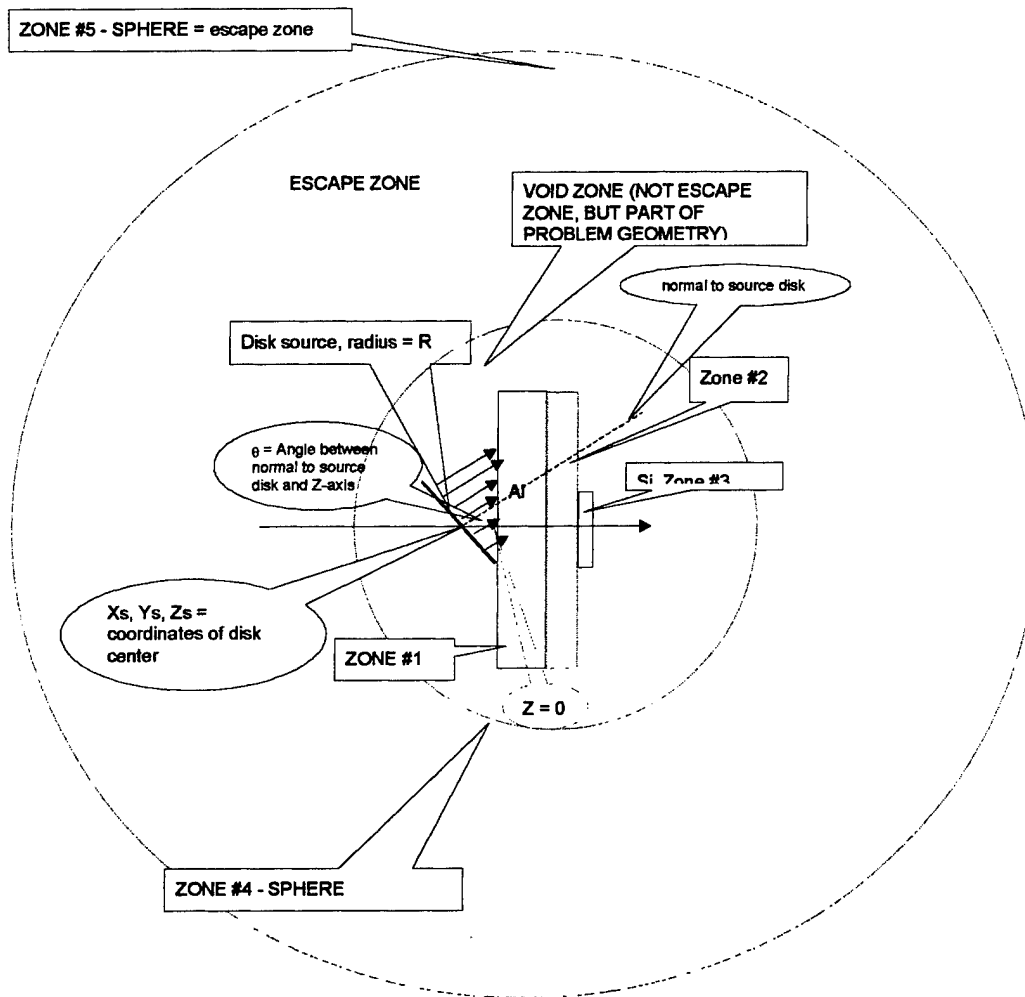


Figure 4. Aluminum / Void / Silicon ACCEPT Problem Geometry (not drawn to scale) With Slant Disk Source as Described in the Input Data File Shown in Figure 5. [Woolf, 2002]

```

TITLE
  3.5 MEV ON AL/VOID/SI, SLANT DISK SOURCE(THETA=45deg) ZS=-.7071
***** GEOMETRY *****
GEOMETRY
*1
  RPP    0.000  5.000  0.000  5.000  0.000  0.635
*2
  RPP    0.000  5.000  0.000  5.000  0.635  0.792
*3
  RPP    2.050  2.950  2.050  2.950  0.792  0.842
*4
  SPH    2.500  2.500  0.421  4.243
*5
  SPH    2.5    2.5    0.421  10.0
END
*ZONES
  Z01 +1
  Z02 +2
  Z03 +3
  Z04 +4 -1 -2 -3
* ESCAPE ZONE IS A VOID SPHERE OF RADIUS  10 CM ENCLOSING THE SLAB
  Z05 +5 -1 -2 -3 -4
END
*MATERIAL
  1
  0
  2
  0
  0
***** SOURCE *****
ELECTRONS
ENERGY  3.5
POSITION  2.5 2.5 -0.7071067
RADIUS  1.0
DIRECTION 45.0 0.0
***** OPTIONS *****
HISTORIES 2000

```

Figure 5. ACCEPT Input Data File for 3.5 MeV 45° Slant Disk Source Incident on Aluminum / Void / Silicon Configuration Shown in Figure 4. [Woolf, 2002]

2.5 Dome Dosimeter Studies

ITS-ACCEPT and MCNPX were used to perform Electron and proton transport calculations for the CEASE DD1 and DD2 dosimeters [Dichter *et al.*, 1998] and PASP Dome D2 and D3 dosimeters [Gussenhoven *et al.* 1995, 1997]. The calculations were made to assist in determining the effects of differences in shield geometry on dose measurements in the same radiation environment. With the differences in shielding geometry taken into account, a common, normalized basis would be provided for the use of measurement data obtained with the CEASE and PASP dosimeters to study the solar cycle dependence of the electron dose from the outer radiation belt.

The CEASE DD1 and DD2 layout diagram, a flat rectangular silicon diode resting on an aluminum oxide substrate mounted on an aluminum base, [Brautigam, 2001] for the is shown in Figure 6. The corresponding ACCEPT geometry schematic is depicted in Figure 7. The dosimeter is capped with an aluminum plate. The DD1 and DD2 assemblies differ only with respect to dimension.

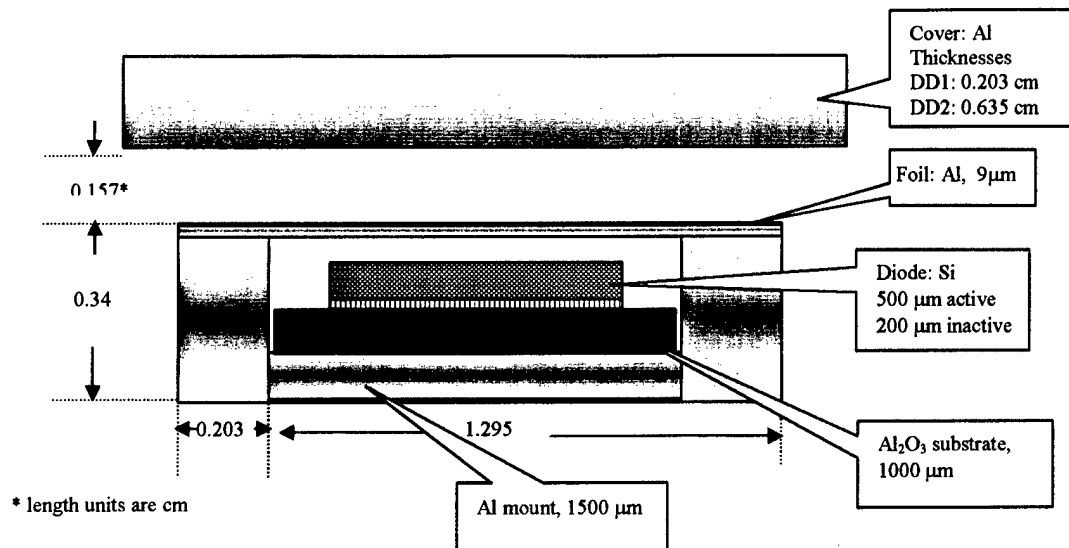


Figure 6. CEASE DD1 and DD2 Dosimeter Assemblies [Woolf, 2002].

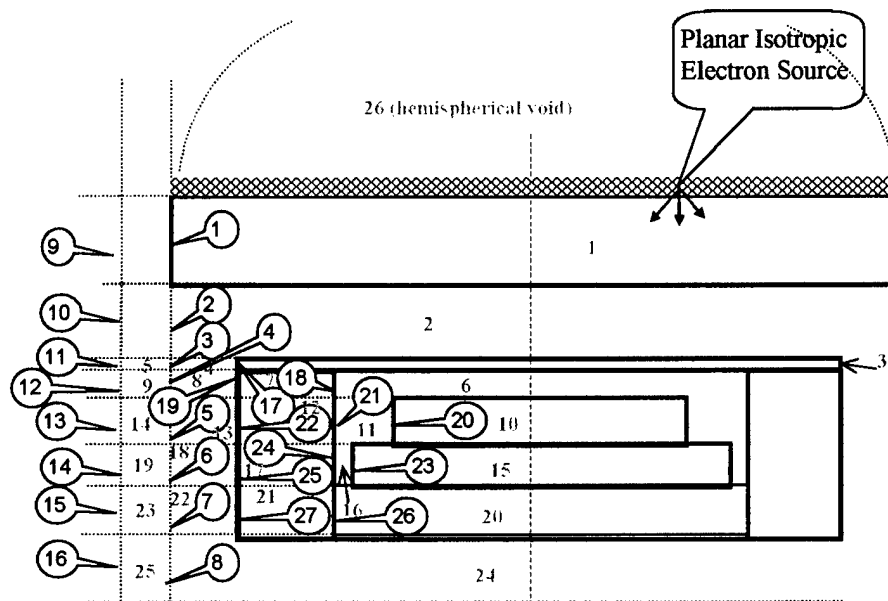


Figure 7. CEASE DD1 and DD2 Dosimeter Geometry Schematic for ACCEPT Showing Plane Isotropic Electron Source; = Geometry Zones; = Material Cells. [Woolf, 2002]

2.6 CEASE Dosimeter Models

Models for the original CEASE DD1 and DD2 geometries were obtained directly using the "CIRCLE-SOURCE" option (see Section 2.4.2). Spatially uniform isotropic source distributions of electrons on the aluminum disc cover (see Figure 6) were assumed. A new source option, "DOME SOURCE," was written for ITS-ACCEPT. For this option, it was assumed that an isotropic, inward-directed electron source is uniformly distributed on the surface of a thin void hemispherical shell of radius equal to that of the disc shield plate as shown in Figure 8. The DD1 and DD2 dosimeters were also studied using MCNPX for a consistency check. The MCNPX geometry schematic is shown in Figure 9. The run files for both ACCEPT and MCNPX simulations are given in Appendices 5 and 6 of Woolf, 2002.

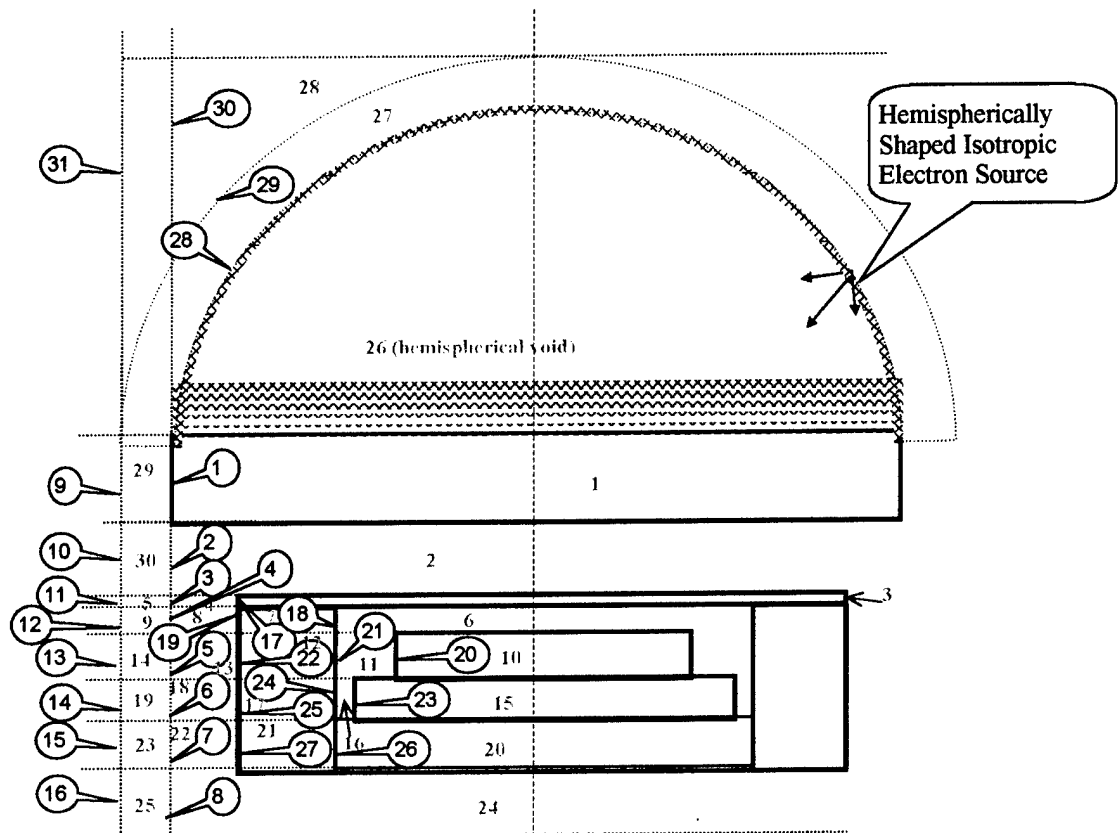

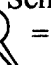


Figure 8. CEASE DD1 and DD2 Dosimeter Geometry Schematic for ACCEPT Showing Hemispherically Shaped Isotropic Electron Source;  = Geometry Zones;  = Material Cells, [Woolf, 2002].

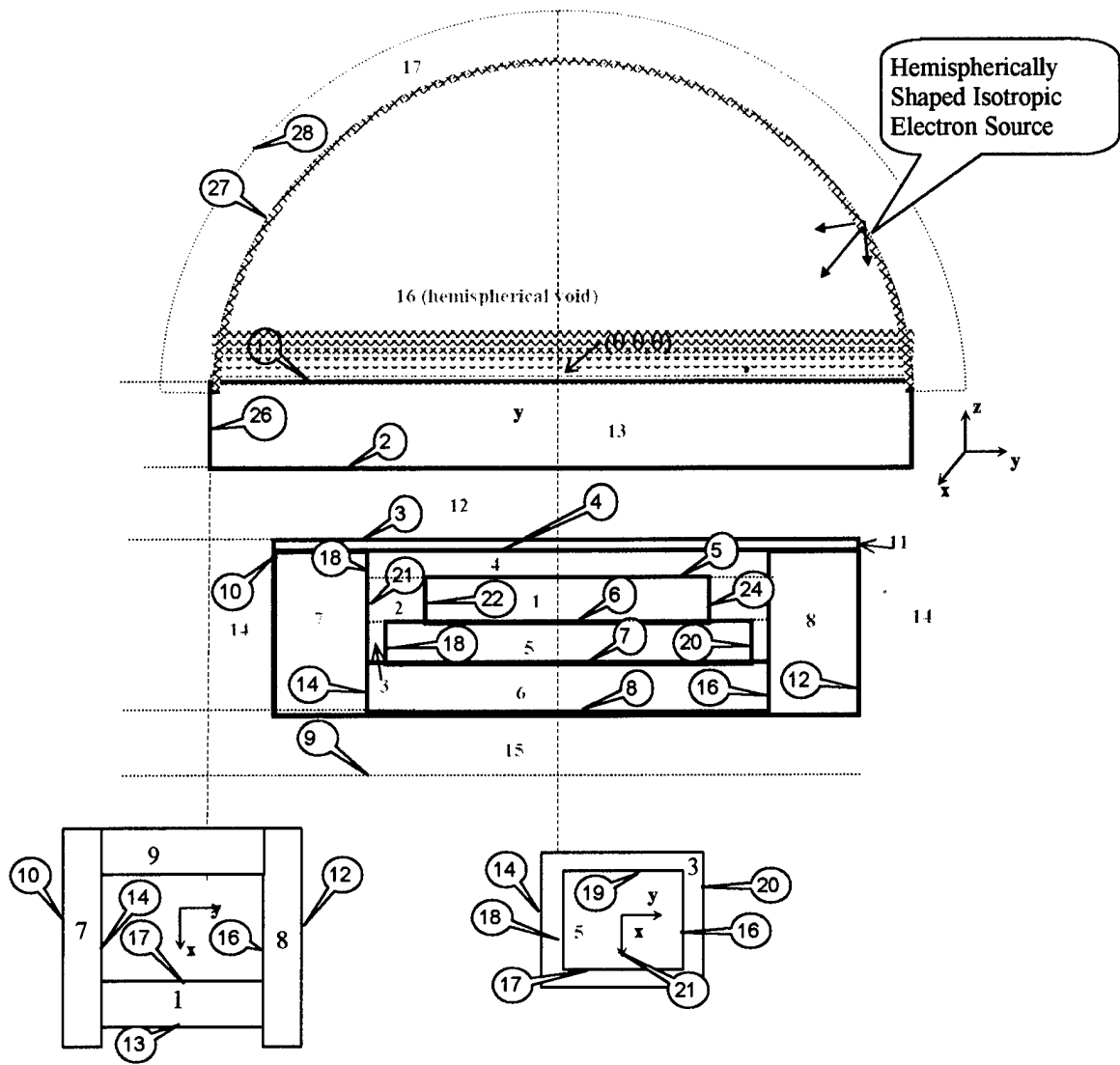




Figure 9. CEASE DD1 and DD2 Dosimeter Geometry Schematic for MCNPX Showing Hemispherically Shaped Isotropic Electron Source;  = Surfaces;  = Material Cells, [Woolf, 2002].

2.7 PASP Dosimeter Models

The ITS-ACCEPT and MCNPX codes were also used to model the PASP dome dosimeters. The geometry schematics and source configurations for PASP Dome 2 for both ACCEPT and MCNPX shown in Figures 10 and 11, respectively. While the use of both ITS-ACCEPT and MCNPX may have been redundant, MCNPX afforded the advantage of a capability for modeling proton transport in addition to electron transport. Electron transport simulations were run at AFRL using the CEASE and PASP dosimeter models described above for several power law electron energy spectra characteristic of the outer belt electron environment. The paper [Brautigam *et al.*, 2001] in which these results are reported comprises Appendix 1 of this report.

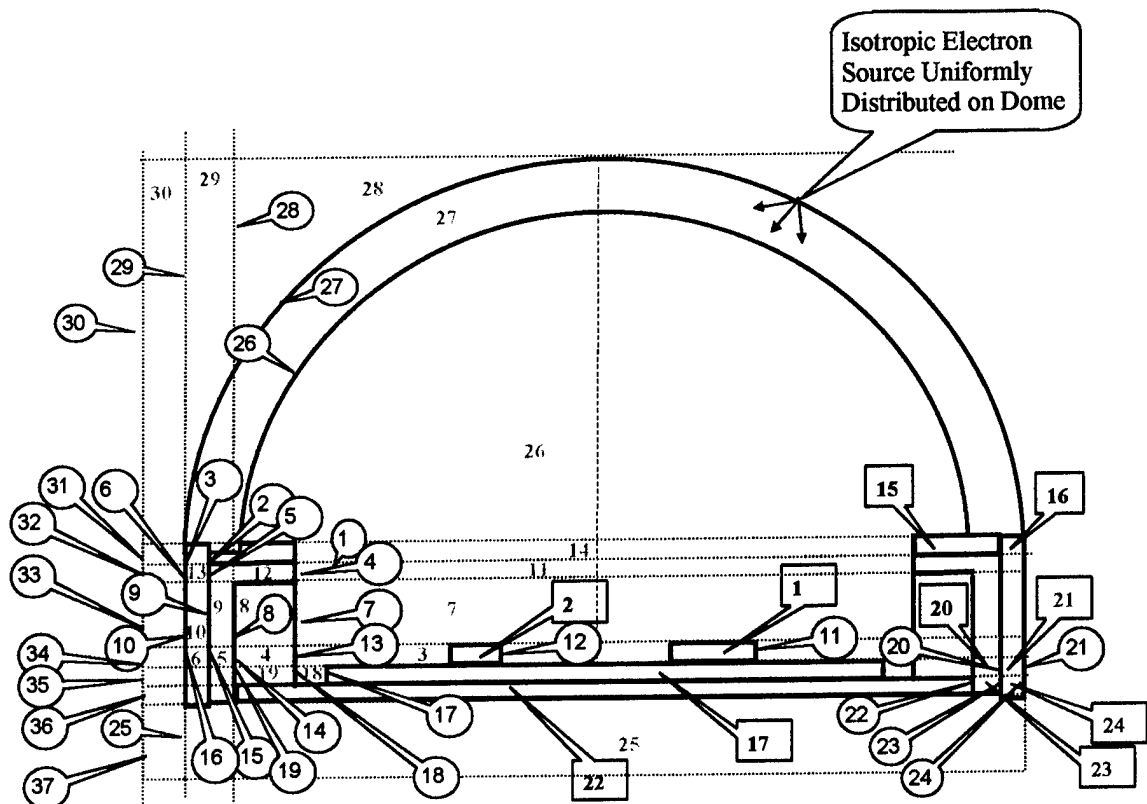
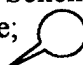



Figure 10. PASP Dome 2 Dosimeter Geometry Schematic for ACCEPT Showing Isotropic Electron Source Incident on Surface of Al Dome;  = Geometry Zones;  = Material Cells, [Woolf, 2002].

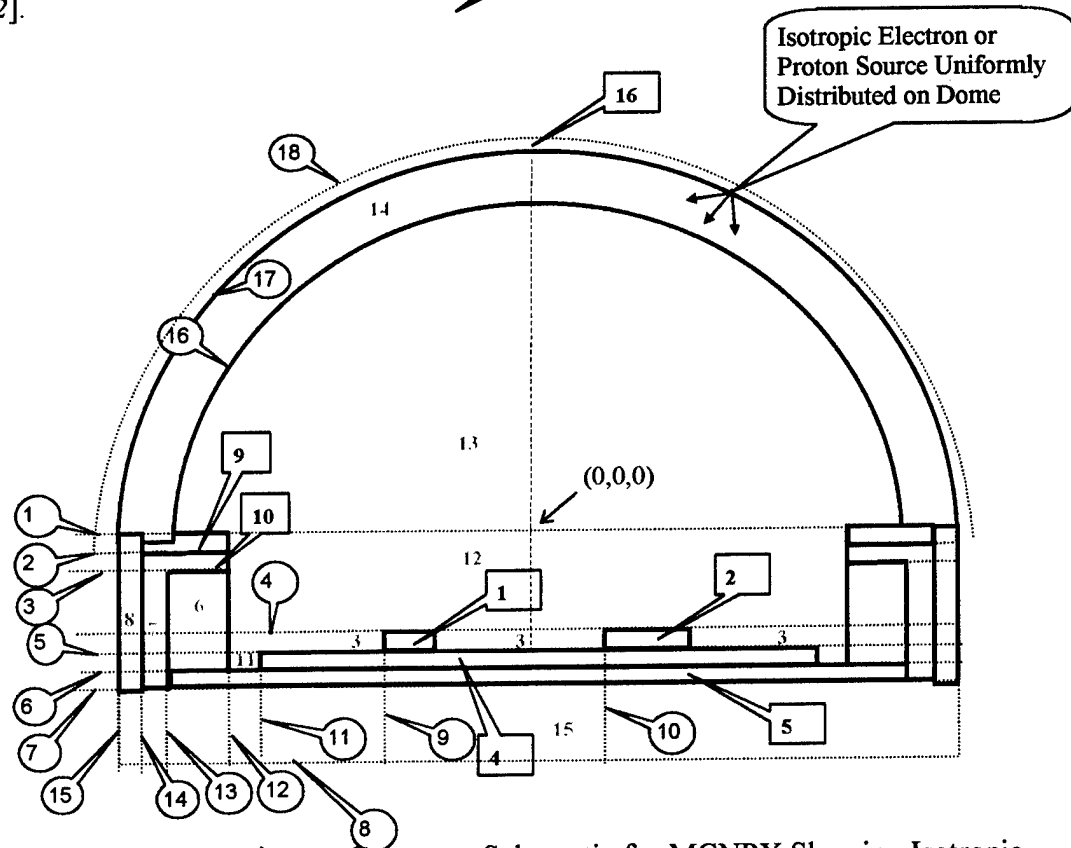




Figure 11. PASP Dome 2 Dosimeter Geometry Schematic for MCNPX Showing Isotropic Electron or Proton Source Incident on Surface of Al Dome;  = Surfaces;  = Material Cells, [Woolf, 2002].

2.8 CRRES Dosimeter Modeling

In 1992, a series of Monte Carlo calculations were made at Los Alamos National Laboratory [*Auchampaugh and Cayton., 1992*] in which flux and dose response functions were obtained for electrons, secondary photons and protons in the CRRES (Combined Release and Radiation Effects Satellite) dosimeters. At the time that these calculations were made, the most up-to-date computer codes available were MCNP [*Briesmeister, 1986*] for electron and photon transport and LAHET [*Prael and Lichtenstein, 1989.*] for the proton transport. Because these codes have since been superseded by MCNPX, we repeated some of the Auchampaugh and Cayton electron/photon transport calculations using both the MCNPX and ACCEPT codes, and in so doing, provided an "in-house" capability for Air Force personnel to perform these and other simulations of this kind.

The original MCNP geometry files from 1992 for the CRRES_D1, D2, D3 and D4 dosimeters, supplied by AFRL [*Brautigam, 2002*] were fed into the visual editor program VISED [*Carter and Schwarz, 1997*] for interpretation, visualization and translation to the code input form of MCNPX and ITS-ACCEPT. Acceptance of the original MCNP input file by MCNPX turned out to be somewhat problematic since there had been several input format changes made since 1992 to the MCNP code family, and there would have been no guarantee that the original file would have been interpreted by MCNPX as originally intended.

The earlier authors, Auchampaugh and Cayton, used a cosine-weighted current source (isotropic flux) and made runs for 17 electron source energies. We modified our dome source option in ITS-ACCEPT to accommodate the cosine-weighted source and duplicated the original 17 runs. The ITS-ACCEPT code was chosen for this task because, on a run-for-run basis, the run time was shorter than that required for MCNPX. The dose response functions calculated in this manner were found to be very close to the original results for electron source energies below 1 MeV. For source energies above 1 MeV, the results were 2-3 orders of magnitude lower than the low energy group and were approximately one order of magnitude higher than the original values. Graphs and a table summarizing these findings are shown in Figure 12 and Table 2.

3. PROTON TRANSPORT MODELING

Throughout the performance of this contract, the MCNPX Monte Carlo program was used to simulate proton transport. These investigations were facilitated by the fact that the same geometry models that were used for the electron transport could be used for the proton work.

3.1 HEP Flight Sensor Simulations of Proton Transport with MCNPX

Several Monte Carlo runs were made, using the MCNPX model of the in-flight version of the HEP instrument (see Section 2.4), of proton transport and energy deposition. A sample MCNPX run file is given in Appendix 4 of Woolf, 2000.

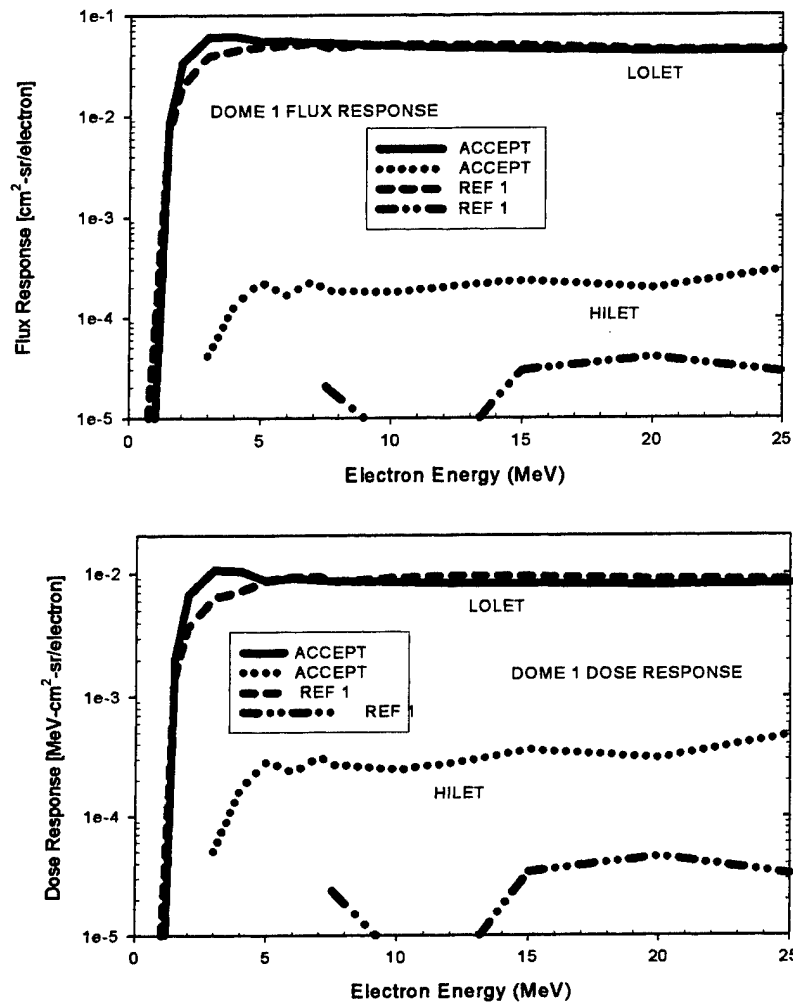


Figure 12. Comparison of Flux and Dose Response Functions Calculated With ITS-ACCEPT and as Reported by Auchampaugh and Cayton [Woolf, 2003].

Table 2. Comparison of ITS-ACCEPT and MCNPX Energy Deposition (MeV) Calculations for
CRRES_D1 Dosimeter for Four Source Energies [Woolf, 2003].

MCNPX CELL #	SOURCE ENERGY = 2 MEV		SOURCE ENERGY = 5 MEV		SOURCE ENERGY = 10 MEV		SOURCE ENERGY = 25 MEV	
	ACCEPT	MCNPX	ACCEPT	MCNPX	ACCEPT	MCNPX	ACCEPT	MCNPX
1	1.975E-04	1.790E-04	2.668E-04	2.898E-04	2.380E-04	2.828E-04	2.215E-04	2.729E-04
2	6.491E-04	6.471E-04	9.164E-04	1.033E-03	7.997E-04	9.973E-04	7.458E-04	9.013E-04
5+6	1.308E+00	1.225E+00	1.875E+00	1.687E+00	2.124E+00	1.836E+00	2.205E+00	1.862E+00
10	6.332E-02	1.054E-01	1.908E-01	2.311E-01	1.943E-01	2.447E-01	1.732E-01	2.360E-01
9	4.008E-02	3.273E-02	8.126E-02	7.564E-02	6.787E-02	7.610E-02	6.147E-02	7.020E-02
11	1.204E-02	2.445E-02	8.851E-02	9.467E-02	8.759E-02	1.057E-01	7.540E-02	1.029E-01
17	6.120E-06	9.523E-03	2.737E-03	1.738E-02	1.665E-02	3.348E-02	1.342E-02	5.948E-02
16	4.050E-05	5.399E-03	1.559E-02	3.233E-02	6.323E-02	7.084E-02	1.204E-01	1.209E-01
15	3.602E-03	5.721E-03	2.902E-01	3.011E-01	1.530E+00	1.397E+00	4.161E+00	4.130E+00
12	2.292E-03	2.124E-03	4.812E-02	3.726E-02	3.963E-02	4.343E-02	3.353E-02	4.116E-02
13	7.183E-03	2.261E-02	1.440E-01	1.457E-01	1.450E-01	1.662E-01	1.216E-01	1.622E-01
14	1.394E-03	2.126E-02	4.484E-01	4.224E-01	4.907E-01	5.142E-01	3.895E-01	4.866E-01
TOTAL	1.439E+00	1.455E+00	3.186E+00	3.046E+00	4.760E+00	4.488E+00	7.355E+00	7.273E+00

3.2 Simulations of Proton Transport in the CEASE Telescope with MCNPX

The model of the CEASE telescope that was written for use with MCNPX (see section 2.1) was also used for studies of proton transport. Calculations of energy deposition in the front (DFT) and back (DBT) silicon wafer detectors of the CEASE telescope were made for eight proton source energies. The source geometry assumed was a disk source covering the telescope aperture with protons exiting the source plane along a direction parallel to the telescope axis. The MCNPX energy deposition results (Figure 13) for the proton sources nearly exactly matched earlier energy deposition calculations supplied to us by AFRL [Brautigam, 2000] (Figure 14).

Proton Energy Deposition
MCNPX simulations

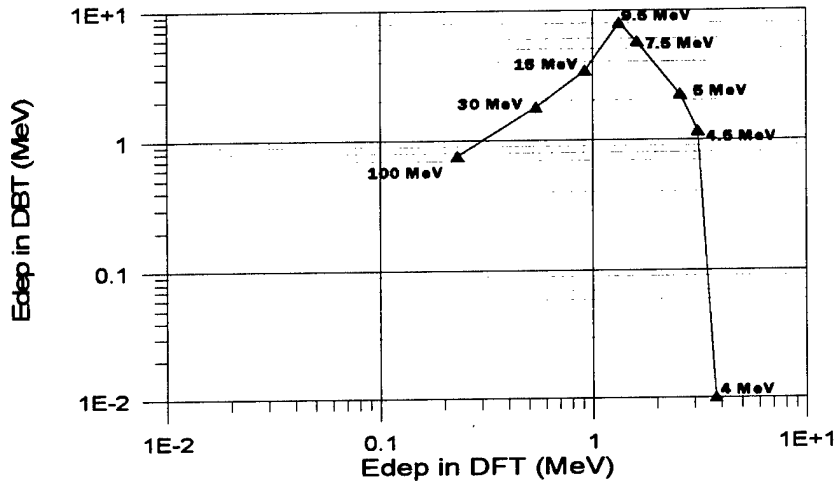


Figure 13. Energy Depositions Due to Protons in DBT vs. DFT for the CEASE Telescope as Computed With the MCNPX Simulation Program [Woolf, 2002].

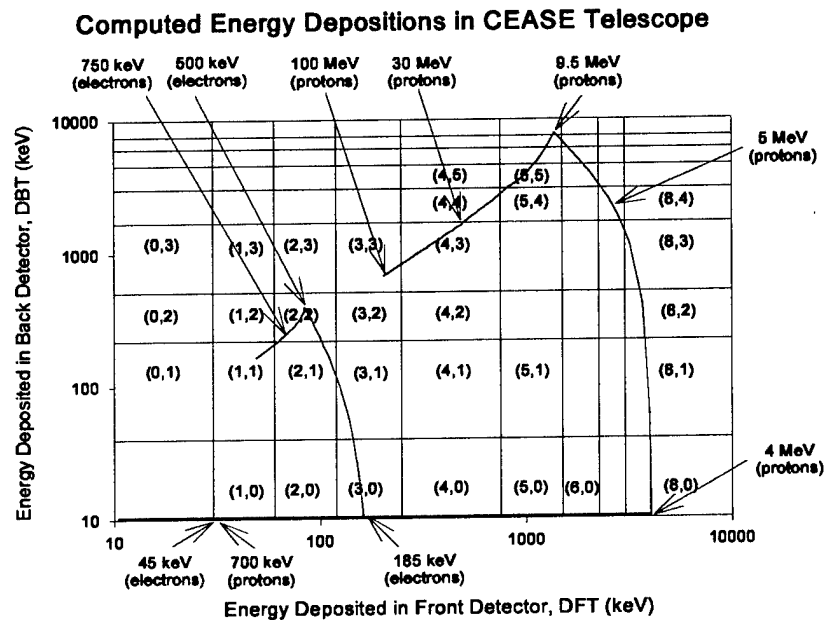


Figure 14. Computed Energy Depositions due to Protons in DBT vs. DFT for the CEASE Telescope [Brautigam, 2000].

Slant source proton transport runs were also made for the CEASE telescope for two 9 MeV proton disk sources (radii 0.025 and 0.05 cm) with 40 degree slant incidence. The pulse height distribution results for the DFT and DBT detectors are shown in Appendix 3 of Woolf, 2003.

In addition to the proton energy deposition calculations, a program was written to identify proton coincidence events in the DFT and DBT detectors by analyzing the individual proton track histories in the transport simulation. The program, "count.F," written for this purpose, performed an audit on the MCNPX track file "ptrac" and identified the history numbers in which the same proton track entered both DFT and DBT. This enabled the investigator to repeat the calculation to examine the details of the identified tracks. Sample output from "count.F" and the program listing may be found in Figure 12 and Appendix 3 of Woolf, 2002, respectively.

3.3 Grazing Angle Proton Scattering Calculations

An investigation was launched to examine the treatment by standard Monte Carlo programs of grazing angle scatter of protons from material surfaces. This work was motivated by the discovery of extensive radiation damage to one of the cameras of the Earth-orbiting Chandra X-Ray Telescope. The cause of the damage to the Chandra telescope was traced to the effect of energetic protons, traveling on trajectories nearly parallel to the telescope's mirrors. Grazing angle scattering off the mirror surfaces led to the transmission of the incident protons to the focal plane and the resulting energy deposition in the focal plane detectors by the transmitted protons. The extent of this damage turned out to be orders of magnitude greater than had been expected. In an attempt to pin down the cause of the damage, intensive simulation studies had been made with the GEANT4 [Giani *et al.*, 2003; Nartallo *et al.*, 2001] Monte Carlo code using models of the Chandra and the European XMM X-Ray telescopes. In our investigation we demonstrated that energetic proton scattering models used in the conventional, well-established Monte Carlo simulation codes, such as GEANT4 and MCNPX, which are appropriate for particles traversing thin foils and transport inside bulk material, are not valid for predicting the scattering of protons with grazing angles of incidence. To accomplish the demonstration, we used MCNPX to treat energetic proton scattering.

A series of proton transport calculations were made with MCNPX, in which the physics of proton scattering is treated in a similar way as is done in Geant4. These runs were made for several proton source beam energies, ranging from 0.05 MeV to 1.0 MeV incident on iridium and aluminum slabs at grazing angles of incidence (0.1° , 0.5° , 1.0°). The emergent, or reflected proton energy-angle spectra (see Figure 14) were examined thoroughly, and it was found that these results did not exhibit the specular reflection [Firsov, 1967] and low loss of energy that would have been necessary to produce the observed radiation damage to the Chandra telescope camera. Moreover, experiments had been performed [Winter *et al.*, 1997; Pfandzelter *et al.*, 1992] in which it had been reported that the grazing incidence protons never actually entered the scattering material, as assumed by standard Monte Carlo codes, but in fact had essentially skimmed the surface. Standard Monte Carlo programs, such as MCNPX and Geant4 treated the scattering and energy loss of grazing incidence protons in the same way as those entering at wide angles. The results of our findings were described in the paper entitled, "Grazing

Angle Proton Scattering: Effects on Chandra and XMM-Newton X-Ray Telescopes", by Bronislaw K. Dichter and Stanley Woolf [*Dichter and Woolf, 2003*].

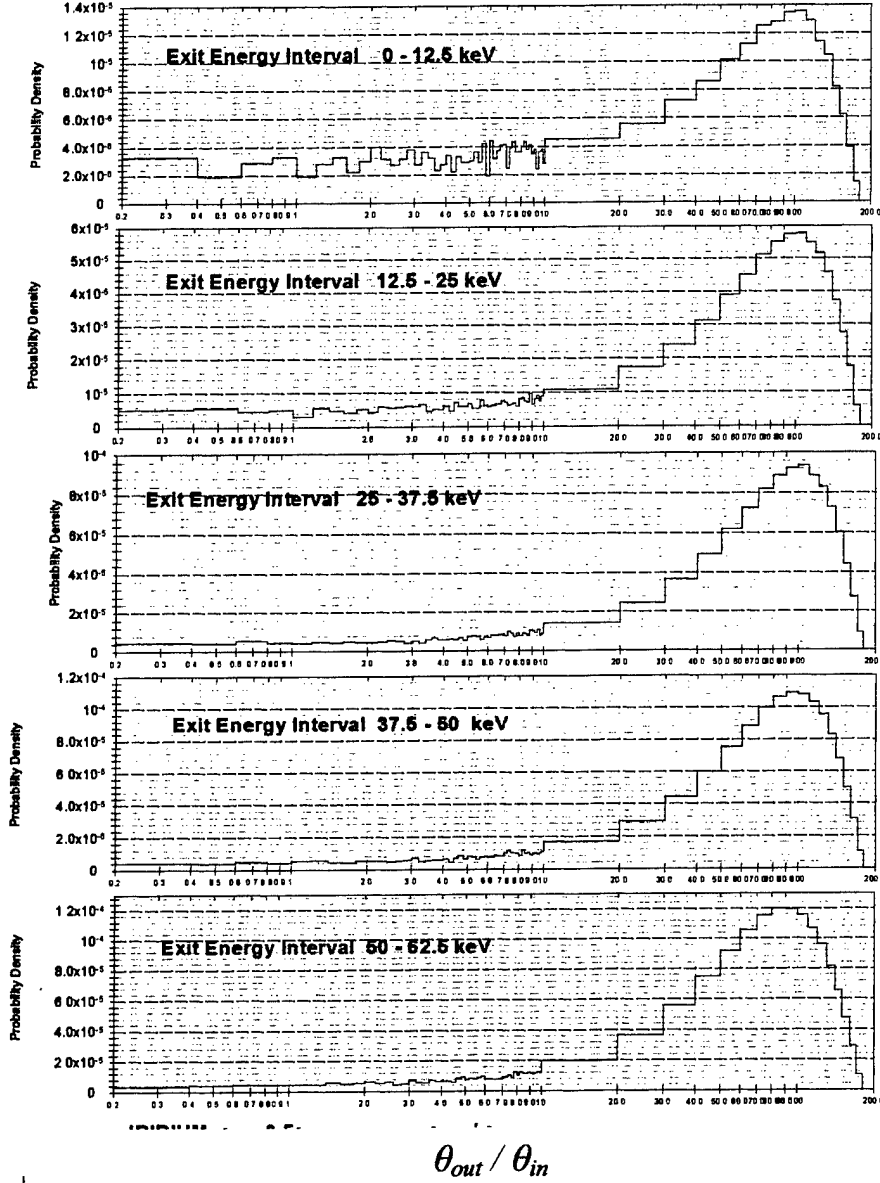


Figure 15. Sample Plots of Probability Density $P_{E_n} \left(\frac{(\theta_{out} - 90^\circ)}{(\theta_{in} - 90^\circ)}; E_{out} \right)$ of Emergent Protons from

Iridium with Exit Polar Angle θ_{out} , for Incident Angle $\theta_{in} = 90.5^\circ$, for Source Energy $E_{in} = 250$ keV and Exit Energy Bins $E_{out} = 0-12.5, 12.5-25.0, 25.0-37.5, 37.5-50.0, 50.0-62.5$ keV [*Woolf, 2003*].

4. SUMMARY

During the period covered by this contract, technical progress was achieved on several fronts related to the research, evaluation and adaptation of particle transport simulation programs for modeling the detection and measurement of space radiation by space-borne sensors. This work included the construction of realistic flight sensor computer models for implementation with several Monte Carlo simulation programs, the performance of several particle transport and energy deposition calculations, simulation of space-borne dosimeters, and studies of the scattering of grazing incidence protons from surfaces of material constituents of space-borne X-ray telescopes. Details of this work are provided in the technical sections of this report and in three interim scientific reports published in December 2000, January 2002, and February 2003, and two technical papers, one published in December 2001 and one to be published in December 2003.

We have made all of the computer codes of various authorship, including our own, available to researchers at the Air Force Research Laboratory. We have provided source code, where applicable, and various materials, including sample files and output data, relating to the use of these codes, and have also engaged in discussions on their use. We also made modifications to some of these Monte Carlo transport codes to render them more appropriate for applications specific to the AFRL Space Vehicles Division.

References

- Auchampaugh, G., Cayton, T., CRRES Dosimeter Simulations, Los Alamos National Laboratory Report No. LA-12511-MS, April 1993.
- Brautigam, D., AFRL/VSBXR, private communication, October 4, 2000.
- Brautigam, D. *et al.*, Solar cycle variation of outer belt electron dose at low earth orbit, *IEEE Trans. Nucl. Sci.* **48**(6), Dec. 2001.
- Brautigam, D., AFRL/VSBXR, private communication, May 15, 2001(a).
- Brautigam, D., AFRL/VSBXR, private communication, May 2002.
- Briesmeister, J. F., Ed., MCNP – A General Monte Carlo Code for Neutron and Photon Transport, Los Alamos National Laboratory Report LA-7396-M, Rev. 2, September 1986.
- Briesmeister, J. F., Ed., MCNP Version 4B2 - A General Monte Carlo Code for Neutron and Photon Transport, Los Alamos Radiation Transport Group(X-6), ORNL RSICC Computer Code Package CCC-200, March 1997.
- Carter, L.L. and Schwarz, R. A., MCNP-UISED 26f- A Visual Editor for Creating MCNP4 Input Files, ORNL RSICC Computer Code Package PSR-358, 1997.
- Dichter, B. K. *et al.*, Compact Environmental Anomaly Sensor (CEASE): A Novel Spacecraft Instrument for *In Situ* Measurements of Environmental Conditions, *IEEE Trans. Nucl. Sci.* **45**(6), 2758, Dec. 1998.
- Dichter, B. K. and Woolf, S. Grazing Angle Proton Scattering: Effects on Chandra and XMM-Newton X-Ray Telescopes, to appear in *IEEE Trans. Nucl. Sci.* **50**(6), Dec. 2003.
- Giani, S. *et al.*, Geant4 Collaboration [Online]. Available: <http://wwwinfo.cern.ch/asd/geant4/geant4.html>, June 2003.
- Gussenhoven, M. S., *et al.*, Low altitude orbit edge of the inner radiation belt: Dose models from the APEX satellite, *IEEE Trans. Nucl. Sci.* **42**(6), 2035, December 1995.
- Gussenhoven, M. S., *et al.*, Low altitude orbit dose as a function of inclination, magnetic activity and solar cycle, *IEEE Trans. Nucl. Sci.* **44**(6), 2161, December 1997.
- Halbleib, J. A. *et al.*, ITS - Integrated TIGER Series of Coupled Electron /Photon Monte Carlo Code System, ORNL RSICC Computer Code Package CCC-467 (March 1992).
- Nartallo, R., Daly, E., Evans, H., Nieminen, P., Lei, F., and Truscott, P., Low-angle scattering of protons on the XMM-Newton optics and effects on the on-board CCD detectors, *IEEE Trans. Nucl. Sci.*, vol. 48, pp.1815-1821, Dec 2001.
- Pfandzelter, R., Stolzle, F., Probing the stopping power near the surface by specular reflection of protons from graphite, NIM B72, pp.163-175, 1992.
- Prael, R. E., Lichtenstein, H., User Guide to LCS: The LAHET Code System, Los Alamos National Laboratory Report LA-UR-89-3014, September 1989.
- Redus, R. H., HEP Flight Model, Amptek, Inc. Bedford, MA, 1998
- Van Riper, K., Sabrina 4.15 for Windows, White Rock Science, P.O. Box 4729, White Rock, NM, 87544, Copyright 2001.

Waters, L. S., Ed., MCNPX™, Version 2.1.5 User's Manual, Los Alamos Radiation Transport Group(X-6), November 14,1999.

Winter, H., Wilke, M., Bergomaz, M., Energy loss of fast protons in grazing scattering from an Al(111)-surface, NIM B125, pp.124-127, 1997.

Woolf, S., Installation and Operation of Particle Transport Simulation Programs to Model the Detection and Measurement of Space Radiation by Space-borne Sensors, Air Force Research Laboratory Report AFRL-VS-TR-2001-1605, December 29, 2000. A398366

Woolf, S., Installation and Operation of Particle Transport Simulation Programs to Model the Detection and Measurement of Space Radiation by Space-borne Sensors, Air Force Research Laboratory Report AFRL-VS-TR-2002-1675, January 3, 2002.

Woolf, S., Installation and Operation of Particle Transport Simulation Programs to Model the Detection and Measurement of Space Radiation by Space-borne Sensors, Air Force Research Laboratory Report AFRL-VS-TR-2003-1547, February 6, 2003.

Appendix A

The paper by Brautigam *et al.* [2001] that comprises Appendix A contains Monte Carlo simulation results that were summarized in Section 2.7 of this report.

Solar Cycle Variation of Outer Belt Electron Dose at Low Earth Orbit

D. H. Brautigam, B. K. Dichter, K. P. Ray, W. R. Turnbull, D. Madden, A. Ling, E. Holeman, R. H. Redus, and S. Woolf

Abstract— The solar cycle dependence of dose rates in the low altitude 'horns' of the outer zone electron belt is examined using data from TSX5/CEASE (solar maximum epoch) and APEX/PASP+ (solar minimum epoch). It is found, after normalizing the dose rates to account for the different shielding geometries, that the ratio of PASP to CEASE dose rates is ~ 4 for $L > 4$. This is contrary to the equal dose rates predicted by the NASA AE8MIN and AE8MAX models.

1. INTRODUCTION

CEASE, the US Air Force Compact Environmental Anomaly Sensor [1], was launched into low earth orbit on the Tri-Service Experiment-5 (TSX5) on 7 June 2000 and began returning data the following day. The experiment was integrated and flown by the DoD Space Test Program, and is expected to operate through October 2001. Its 13 months of operation to date has spanned a period of solar maximum peak activity. The TSX5 low earth orbit is similar to that of the APEX spacecraft on which the PASP+ dosimeter [2],[3] operated during the two years (1994 to 1996) leading up to solar minimum. These two data sets provide the opportunity to study the solar cycle dependence of the outer radiation belt electron dose.

It is well known that the highly variable outer radiation belt MeV electron population contributes to spacecraft system degradation through deep dielectric charging and radiation dose [4],[5]. This particle population also represents a radiation hazard to astronauts, particularly if extravehicular activities are scheduled during magnetically disturbed conditions when the outer radiation belt is inflated with intense fluxes [6]. Thus, there is a great incentive to improve understanding of the dynamics of this particle population, and develop more accurate models with which to specify this environment.

Geosynchronous spacecraft provide the necessary long-term continuous database for studying solar cycle variations of the outermost boundary of the outer belt. Such studies have found that during the two to three years preceding solar minimum, the MeV electrons at geosynchronous altitude exhibit episodic enhancements with a 27-day periodicity attributed to the well structured high speed solar wind streams (HSSWS) which flow from coronal holes near the solar ecliptic plane during this phase of the solar cycle [7],[8],[9]. This periodic behavior has also been observed in dose measurements at low altitude polar orbit [10],[11],[12]. This pre-solar minimum enhanced activity results in yearly-averaged geosynchronous fluxes of >3 MeV electrons which can be ~ 8 times higher than the corresponding averages around solar maximum [9].

The trapped electron environment has been characterized by long-term average models (NASA solar minimum AE8MIN and maximum AE8MAX [13]) and magnetic activity dependent models (APEXRAD [3], CRRESRAD [14], and CRRESELE [15]). The solar cycle phase dependence of geosynchronous electrons referred to earlier is inconsistent with the NASA AE8 electron models which show that the geosynchronous ($L=6.6$) integral flux of >3 MeV electrons during solar maximum and solar minimum are equivalent [13]. Other deficiencies of currently available models have been previously discussed [16],[17]. Spacecraft design engineers are interested in not just long-term average radiation belt models (either current or some future improved version), but models which give the probability of encountering various levels of radiation as a function of solar cycle phase.

This study examines the solar cycle dependence of dose in the low altitude, high latitude 'horns' of the outer zone electron belt. Both mission-average dose and probability distribution models are created for the APEX and TSX5 epochs which encompass solar minimum and maximum, respectively. These models show that for the epochs studied, the outer zone average dose rate from electrons is a factor of ~ 4 higher (for $L > 4$), and peak at higher L , during solar minimum than during solar maximum. Section II describes the relevant details of the spacecraft orbits and dosimeters, and section III discusses the construction of the models. Section IV discusses the results, and section V concludes with a summary.

Manuscript received July 16, 2001. This work was sponsored by AFRL under contract Nos. F19628-00-C-0073 (Boston College), F19628-96-C-0063 (Amptek), F19628-00-C-0089 (Radex), and F19628-99-C-0077 (Arcon).

D.H. Brautigam, B.K. Dichter, K.P. Ray, W.R. Turnbull, are with the Air Force Research Laboratory, Space Vehicles Directorate, Hanscom AFB, MA 01731 USA (e-mail: Donald.Brautigam@hanscom.af.mil).

D. Madden and E. Holeman are with Institute for Scientific Research, Boston College, Boston, MA USA.

R.H. Redus is with Amptek, Inc., Bedford, MA 01730 USA.

A. Ling is with Radex, Inc., Bedford, MA 01730 USA.

S. Woolf is with Arcon, Corp., Waltham, MA 02451 USA

II. SATELLITE ORBITS AND DOSIMETERS

The APEX satellite was launched on 5 August 1994 into a 70° inclination orbit with a perigee of 362 km, an apogee of 2544 km, and an orbital period of 115 minutes. The mission had some downtime, but remained active through May 1996 (solar minimum), with the PASP+ dosimeter returning approximately 12 months of data. The TSX5 satellite was launched on 7 June 2000 into a 69° inclination orbit with a perigee of 410 km, an apogee of 1710 km, and an orbital period of 105 minutes. The CEASE dosimeter has been returning data continuously (with occasional minor data gaps) to date, resulting in more than 12 months of data for analysis. The solar cycle phase of the APEX and TSX5 satellite epochs are shown in Fig. 1. The APEX epoch spans the ~2 years leading into solar minimum (May 1996), and the TSX5 epoch includes ~1 year about solar maximum.

Both the PASP+ and CEASE dosimeters are constructed with an electrically active silicon diode sensor behind an aluminum (Al) shield of a prescribed thickness which determines the threshold energy of particles which can penetrate the shield and deposit energy in the silicon sensor. The PASP+ dosimeter instrument includes four individual dosimeter heads (D1,D2,D3,D4) providing measurements from a range of particle energies [2],[3]. The D2 dosimeter head includes two different sized silicon diode sensors beneath an aluminum dome shield, D2B being the larger of the two. The CEASE instrument includes two dosimeter heads DD1 (thin shield) and DD2 (thick shield) [1]. Table 1 summarizes the main characteristics of the PASP+ D2B dosimeter and the CEASE DD1 dosimeter (which for simplicity will be referred to from hereon as PASP and CEASE, respectively) which are relevant to this study. Although the Al shield thickness for the two dosimeters is comparable, the geometry is different; PASP is constructed with a hemispherical dome shield and CEASE with a planar shield. Particles following straight line paths towards the sensor from any point within the two pi field of view outside the PASP dome will pass through equal pathlengths of Al shield. Although the planar dosimeter does not exhibit this spherical symmetry it represents a more realistic geometry for simulating spacecraft shielding designs. The PASP and CEASE silicon diodes are of comparable thickness, yet the CEASE diode has a much greater planar dimension. The Low Linear Energy Transfer (LoLET) channel is defined by its energy deposition threshold settings (0.05 to 1.0 MeV for PASP and 0.05 to 0.85 MeV for CEASE). For ~80 mils of Al shielding, electrons above ~1 MeV and protons above 78 MeV (for CEASE) to 115 MeV (for PASP) can penetrate the shielding and deposit the required energy for the LoLET channel. Although the >1 MeV electrons are the dominant source of LoLET dose in the outer radiation belt, the sporadic solar energetic proton events (most frequent during solar maximum) may contribute a relatively significant short term LoLET dose over the course of a 2 to 3 day event. These

events have been identified and are excluded from the database for this study.

Dose measurements are dependent on shielding characteristics (material, thickness, and geometry) and thus do not provide a direct measure of the environment as does a flux measurement which discriminates particle species and energy. In order to substantiate any claim about the variable electron environment based on the comparison between two different dosimeter measurements on separate spacecraft, it is important to 'normalize' their dose values to some reference. The relative response of the two dosimeters is investigated using the Integrated Tiger Series (ITS) electron transport code [18]. In this simulation, an isotropic power law spectrum (1 to 10 MeV) is uniformly emitted from a virtual hemispherical surface centered on the dosimeter sensor. Simulations are performed for a range of power law indices ($N=2$ to 6) which are representative of the outer belt electron environment. The results show that for the hardest incident flux spectrum ($N=2$) the dose ratio for the hemispheric to planar dosimeter is 2.0, and increases monotonically to 2.4 for the softest spectrum ($N=6$), for an average ratio of 2.2. Because the planar dosimeter better represents spacecraft surface geometry, and because a number of CEASE units are planned for future flights, CEASE is taken as the reference standard here, and the PASP (hemispheric) dose is normalized to CEASE dose by dividing by a factor of 2.2.

Another issue to consider when comparing particle data from different instruments, even from the same spacecraft, is their field of view (FOV) relative to the geomagnetic field. This determines the particle pitch angle distribution being sampled (the pitch angle is the angle between the particle velocity and the local geomagnetic field vectors). A collimated particle telescope pointing in a direction orthogonal to the geomagnetic field can see orders of magnitude higher particle fluxes (at 90° pitch angle) than an identical instrument pointing parallel (anti-parallel) to the field line at 0° (180°) pitch angle. The APEX and TSX5 spacecraft are both 3-axes stabilized. The APEX attitude control system maintained a solar inertial reference with PASP pointing nearly parallel (within 5°) to the ecliptic plane and orthogonal to the Earth-Sun line. The TSX5 attitude control system maintains a geocentric reference with CEASE pointing in a direction orthogonal to the spacecraft velocity vector and pointing 30° from the zenith direction. Assuming a collimated FOV direction normal to the dosimeter face (in actuality, each dosimeter has a full two pi steradian FOV), a pitch angle histogram was created and a mission average computed for each dosimeter. With the 0-180° pitch angle distribution collapsed to a 0-90° distribution, the average values were found to be 35° (CEASE) and 50° (PASP) over the range from L equal 3 to 6.5. This marginal difference in average pitch angle represents a negligible effect, particularly given the fact that the two dosimeters are not collimated but have a full two pi steradian FOV. The difference in PASP and

CEASE orientation is thus assumed to be an insignificant factor in comparing the daily average dose rates.

III. ANALYSIS

Since radiation belt particle motion is tied to the geomagnetic field, magnetic coordinates ($L, B/B_0$) are the logical choice for ordering the dose data. The coordinate 'L' labels a magnetic field line by the radial distance (in Earth radii) at which it crosses the magnetic equator. The coordinate ' B/B_0 ' is the ratio between the magnetic field B at some arbitrary point along a field line and the equatorial (minimum) value B_0 along that same field line. The CEASE and PASP dose databases are binned and averaged in ($L, B/B_0$) in a manner identical to the published APEXRAD model (see [2],[3] for details). The resulting mission averaged APEX/PASP and TSX5/CEASE dose rate maps, when displayed on the northern quadrant of a dipolar grid (Fig. 2), aid in visualizing the relevant spatial regions. The inner zone is seen as the darker color contours extending from the equator inside $L=1.5$, while the outer zone 'horns' are seen as darker color contours at high latitudes in the region between $L=3$ to 5. The heart of the outer radiation belt is the equatorial projection of the $L=3$ to 5 field lines and exhibit much higher dose rates than those at the low altitudes shown in Fig. 2.

Since the APEX and TSX5 orbits are not identical, regions of ($L, B/B_0$) space are sampled differently by the two spacecraft. Simply averaging over the entire range of B/B_0 for a fixed L would yield skewed results because of the different temporal coverage in ($L, B/B_0$) and the dose dependency on B/B_0 . To best compare dose variations seen by PASP and CEASE, a subset of the complete ($L, B/B_0$) grid is determined which provides ample observations for the study, yet also minimizes the spread in B/B_0 for a fixed L bin width ($0.1 R_E$). The bottom panel of Fig. 3 illustrates the increasing B/B_0 bin width as a function of L . The top panel illustrates the range of altitudes sampled by the respective satellites corresponding to the specified L and B/B_0 range. For $L < 5.5$ the coverage in altitude is quite constant, where the average range for APEX altitudes is 1355 ± 520 km, and for TSX5, 1270 ± 350 km. Fig. 2 illustrates roughly the region of interest as being enclosed between the $L = 3$ to 5 field lines and between the 1000 to 2000 km altitude arcs. In what follows, it should be understood that within the explicit L dependence of dose distributions is an implicit dependence in B/B_0 .

Subsequent to binning the full resolution (5s) dose data into the ($L, B/B_0$) grid prescribed above, the daily averaged dose rates for both data sets are computed as a function of L . These daily dose profiles are plotted as epoch surveys in Fig. 4a (APEX/PASP) and Fig. 4b (TSX5/CEASE), along with the respective magnetic activity index Dst history for each epoch. The PASP dose survey, particularly up through 1995.5, highlights the periodic enhancements of MeV electrons characteristically observed during the years approaching solar minimum. Dst is a measure of magnetic storm activity, with a more negative value indicative of greater activity. Periods

exhibiting the largest Dst excursions (e.g., during the TSX5 epoch around years 2000.55 and 2001.25) also show the largest increases in dose rates in the slot region (down to $L=2.5$).

The simplest way to compare the dose rates from the two different epochs is to construct a single average dose model as an explicit function of L from each mission. These average dose profiles are presented in Fig. 5. The average PASP (solar minimum epoch) dose rate is higher and peaks at a higher L value than that for CEASE (solar maximum epoch). The PASP peak dose rate is 1.1×10^{-4} rd/s (at $L=4.1$), while the CEASE peak dose rate is 3.2×10^{-5} rd/s (at $L=3.8$). The ratio of PASP to CEASE dose rate decreases from ~ 5 for $L=4.5$ to ~ 3 at $L=6.5$. The PASP dose rate peak is also somewhat narrower than the CEASE peak. For comparison, average dose rates at several ($L, B/B_0$) points are computed using spectra from the NASA AE8 models (the AE8 models were downloaded from the web pages of NASA's National Space Science Data Center). For a given L , the values of B/B_0 used to specify the AE8MIN (AE8MAX) spectra are the average B/B_0 from the corresponding APEX (TSX5) ephemeris. The ITS code is used to simulate the transport of the AE8MIN and AE8MAX omnidirectional flux spectra (1 to 7 MeV) through the PASP and CEASE dosimeter models, respectively. These AE8 model predicted dose rates are included in Fig. 5. For $L > 4$, the AE8MAX and AE8MIN models give identical fluxes for a given coordinate pair ($L, B/B_0$). However, due to the slight differences in the average B/B_0 for the two spacecraft orbits, the AE8MIN and AE8MAX dose predictions for $L > 4$ differ by $\sim 30\%$, the difference attributed to the variation of spectra with B/B_0 . For $L \leq 4.5$ the AE8MIN model is less than a factor of 2 higher than the observed PASP dose. For $L > 4$ the ratio of AE8MIN to PASP increases steadily to ~ 5 near geosynchronous. The agreement between AE8MAX and CEASE is much less, with the ratio of AE8MAX to CEASE increasing steadily from ~ 6 at $L=3.5$ to ~ 10 near geosynchronous.

In addition to long-term average dose models which obscure the wide dynamic variations of the outer belt electrons, space system design engineers are interested in the probability of exceeding a given dose rate at a fixed point in space. To construct these distributions, the observed dynamic range of dose rates (spanning five orders of magnitude, 10^{-7} to 10^{-2} rd/s) is divided into 50 equal logarithmically spaced bins. For each L bin, the fraction of 5s dose measurements falling within each dose rate bin is determined such that the integral over all dose rate bins sums to 1. The probability for exceeding a given dose rate D is then determined by integrating over these dose rate bins from D to D_{\max} ($=10^{-2}$ rd/s). These probability distributions, for both APEX and TSX5 missions, for all L , are shown in Fig. 6(a;b). The shape of the dose profiles (in L) seen in Fig. 5 is reflected in Fig. 6. To facilitate a direct comparison of the probability distributions for the two epochs, the distributions at a single L near the dose peak ($L=4$) are plotted together in Fig. 7. From

this plot, it can be seen that for these missions, the probability of exceeding the dose rate of 10^{-4} rd/s is ~ 0.38 during the solar minimum epoch (APEX) and ~ 0.10 during the solar maximum epoch (TSX5). It should be emphasized that these probabilities have been derived from a specific range of $(L, B/B_0)$ space. For the case here of $L=4$, B/B_0 ranges between 48 and 80, and is not representative of the dose environment for $L=4$ on the equator ($B/B_0=1$) where dose rates are considerably larger.

IV. DISCUSSION

One clear result here is that for $L>4$, the mission averaged PASP (solar minimum epoch) dose rates are a factor of ~ 4 higher than those for CEASE (solar maximum epoch), a significant departure from the nearly equal rates predicted by the NASA AE8 models. This result is consistent with recent studies which attribute periodic enhancements of MeV electron flux at geosynchronous to the HSSWS prominent during the approach towards solar minimum [7],[8],[9]. This 27-day periodicity in enhancements of MeV electrons is evident in the PASP dose seen in Fig. 4a, where the enhanced dose rates are observed throughout a wide range of L spanning the 'horns' of the outer radiation belt.

A second result is that the average dose profile for CEASE (solar maximum epoch) peaks at a lower L ($L=3.8$) and has a broader peak than does the dose profile for PASP (solar maximum epoch) which peaks at $L=4.1$. This result is attributed to the greater number of magnetic storms occurring during solar maximum. The difference in geomagnetic activity for the two epochs is apparent in the plots of Dst in Fig. 4, where maximum negative excursion in Dst corresponds to the severest magnetic storm activity. Although there were comparable numbers (~ 6) of moderate storms ($Dst = -100$ to -150 nT) during both epochs, there were 8 major storms ($Dst < -150$ nT) during the TSX5 epoch, with none during the APEX epoch. Associated with these largest storms are the injections of dose producing electrons which penetrate deep into the slot region ($L \sim 2.5$). The greater frequency of these storms during solar maximum moves the inner edge of the average dose profile to lower L and broadens the profile peak.

Future work will investigate the possibility of extending the spatial coverage of *in situ* dose measurements by developing algorithms for mapping dose along field lines to other remote regions and by interpolating between other existing spacecraft. Although this study dealt with the LoLET dose behind 80 mils of Al corresponding to >1 MeV electrons, future work will analyze a second CEASE channel for dose behind 250 mils of Al corresponding to >3 MeV electrons. The relative dose from these two channels may then be used to examine the spatial-temporal variability of spectral hardness of this very dynamic trapped particle population.

V. SUMMARY

The significance of the outer zone electrons, both in terms of their effect on space technologies [4],[5] as well as human safety [4],[6], is well known. However, much work is required to better characterize this population's variability over solar cycle time scales. Whereas long-term averages were once the model standard, it is becoming increasingly evident that more detailed information on the extremes and the variability of the environment is advantageous for both satellite design engineers and those responsible for planning human activities in space.

This study has produced results that are consistent with studies utilizing geosynchronous flux data which found that electron enhancements minimize near solar maximum and maximize during the approach to solar minimum. The discrepancy with the NASA AE8 models underscores the need to promote further improvement of existing radiation models by continually monitoring the radiation belts throughout the solar cycle. This study has also produced some probabilistic models as a step towards an alternative to the standard mission averaged model. Although the study's spatial coverage is limited to low Earth orbit, and its temporal coverage to <3 years of an 11-year solar cycle, it does provide a framework for incorporating future data sets. More CEASE units are scheduled to fly in the future, and these data will continue to expand the current spatial-temporal coverage leading to improved modeling capabilities.

VI. ACKNOWLEDGMENT

D.H.B. would like to thank E.G. Mullen and M.S. Gussenhoven for valuable discussions and for laying the groundwork for this study over their many years at AFRL.

VII. REFERENCES

- [1] B.K. Dichter, J.O. McGarity, M.R. Oberhardt, V.T. Jordanov, D.J. Sperry, A.C. Huber, J.A. Pantazis, E.G. Mullen, G. Ginot, and M.S. Gussenhoven, "Compact Environmental Anomaly Sensor (CEASE): A novel spacecraft instrument for *in situ* measurements of environmental conditions," *IEEE Trans. on Nucl. Sci.*, vol. 45, no. 6, pp. 2758-2764, 1998.
- [2] M.S. Gussenhoven, E.G. Mullen, D.A. Hardy, D. Madden, E. Holeman, D. Delorey, and F. Hanser, "Low altitude edge of the inner radiation belt: Dose models from the APEX satellite," *IEEE Trans. on Nucl. Sci.*, vol. 42, no. 6, pp. 2035-2042, 1995.
- [3] M.S. Gussenhoven, E.G. Mullen, J.T. Bell, D. Madden, and E. Holeman, "APEXRAD: Low altitude orbit dose as a function of inclination, magnetic activity and solar cycle," *IEEE Trans. on Nucl. Sci.*, vol. 44, no. 6, pp. 2161-2168, 1997.
- [4] J. Feynman and S.B. Gabriel, "On space weather consequences and predictions," *J. Geophys. Res.*, vol. 105, pp. 10543-10564, 2000.
- [5] A.R. Frederickson, "Upsets related to spacecraft charging," *IEEE Trans. on Nucl. Sci.*, vol. 43, no. 6, pp. 426-441, 1996.
- [6] Space Studies Board, National Research Council, Radiation and the International Space Station: Recommendations to Reduce Risk, National Academy Press, 2000.
- [7] D.N. Baker, J.B. Blake, R.W. Klebesadel, and P.R. Higbie, "Highly relativistic electrons in the Earth's outer magnetosphere: 1. Lifetimes and temporal history 1979-1984," *J. Geophys. Res.*, vol. 91, pp. 4265-4276, 1986.

- [8] G.L. Wren, D.J. Rodgers, and P. Buehler, "Modeling the outer belt enhancements of penetrating electrons," *J. Spacecraft and Rockets*, vol. 37, 408-415, 2000.
- [9] D. N. Baker, R. A. Goldberg, F. A. Herrero, J. B. Blake, and L. B. Callis, "Satellite and rocket studies of relativistic electrons and their influence on the middle atmosphere," *J. Spacecraft and Rockets*, vol. 55, no. 13, pp.1619-1628, 1993.
- [10] M.S. Gussenhoven, E.G. Mullen, R.C. Filz, and D.H. Brautigam, "New low altitude orbit measurements," *IEEE Trans. on Nucl. Sci.*, vol. 34, no. 6, pp. 676-683, 1987.
- [11] M.S. Gussenhoven, E.G. Mullen, D.H. Brautigam, and E. Holeman, "Dose variation during solar minimum," *IEEE Trans. on Nucl. Sci.*, vol. 39, no. 6, pp. 1671-1677, 1991.
- [12] M.S. Gussenhoven, E.G. Mullen, and E. Holeman, "Radiation belt dynamics during solar minimum," *IEEE Trans. on Nucl. Sci.*, vol. 36, no. 6, pp. 2008-2014, 1989.
- [13] J.D. Gaffey Jr., and D. Bilitza, "NASA/National Space Science Data Center Trapped Radiation Models," *J. Spacecraft and Rockets*, vol. 31, 172-176, 1994.
- [14] K.J. Kerns and M.S. Gussenhoven, "CRRESRAD Documentation," PL-TR-92-2201, Phillips Laboratory, AFMC, Hanscom, AFB, MA, 1992.
- [15] D.H. Brautigam, M.S. Gussenhoven, and E.G. Mullen, "Quasistatic model of outer zone electrons," *IEEE Trans. on Nucl. Sci.*, vol. 39, no. 6, pp. 1797-1803, 1992.
- [16] E.J. Daly, J. Lemaire, D. Heynderickx, and D.J. Rodgers, "Problems with models of the radiation belts," *IEEE Trans. on Nucl. Sci.*, vol. 43, no. 2, pp. 403-415, 1996.
- [17] M.S. Gussenhoven, E.G. Mullen, and D.H. Brautigam, "Near-earth radiation model deficiencies as seen on CRRES," *Adv. in Space Res.*, vol. 14, no. 10, pp. 927-941, 1994.
- [18] J. A. Halbleib et al., "TIS - Integrated TIGER Series of Coupled Electron / Photon Monte Carlo Code System," ORNL RSICC Computer Code Package CCC-467

TABLE I
DOSIMETER CHARACTERISTICS

Dosimeter	Shield (Al)	Sensor (Si)		LoLET (MeV)	
Sensor head	Thick (mil) geometry	Area (cm ²)	Depth (cm)	Energy deposit	Electron threshold
PASP	82.5	0.051	0.038	0.05-1.0	≥ 1.0
D2B	dome				
CEASE	80.0	0.810	0.050	0.05-0.85	≥ 1.0
DD1	planar				

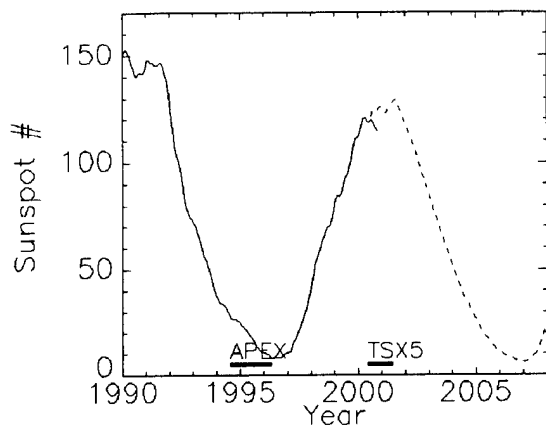


Fig. 1. The solar cycle is depicted here in terms of the smoothed sunspot number. The dashed curve beginning in mid-2001 is the predicted value. The mission time intervals for APEX (~2 years leading into solar minimum) and TSX5 (~1 year at solar maximum) are indicated by the heavy solid lines.

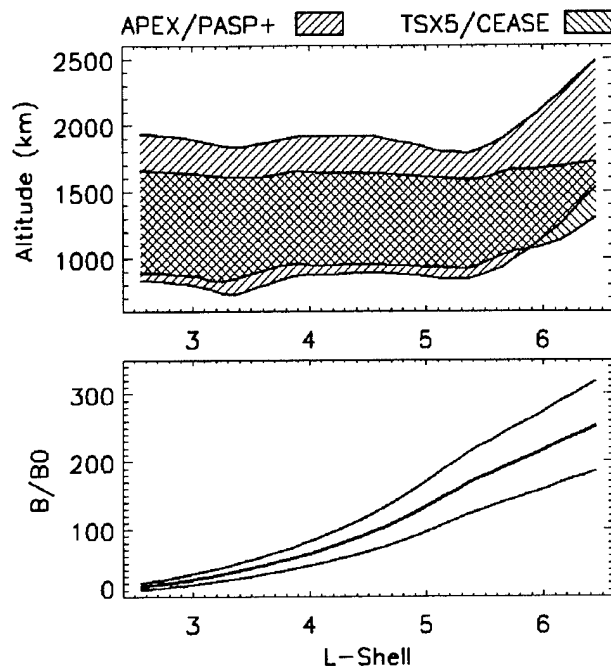


Fig. 3. Dose data are sorted by $(L, B/B_0)$ coordinates. The L bin width is fixed at $0.1 R_E$, whereas the B/B_0 bin width increases with L . In the bottom panel the average $B/B_0(L)$ for the two spacecraft is plotted (heavy solid line) versus L , with the upper and lower limits of the $B/B_0(L)$ bin width defined by ± 0.25 of the average. In the top panel the altitude coverage (\pm one sigma of the average value) of satellites is plotted versus L .

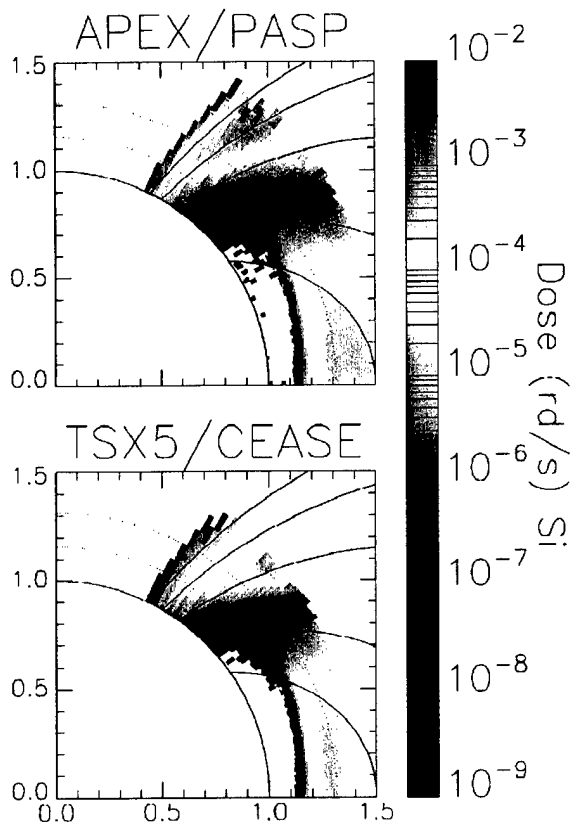


Fig. 2. Mission average dose rates (rd/s) in silicon (color coded) plotted in dipole $(L, B/B_0)$ coordinates for PASP (top) and CEASE (bottom). The vertical and horizontal scales are in units of Earth radii. Dipole field lines for $L = 1.5, 2, 3, 4$, and 5 have been drawn, with the $L=1.5$ field line shown intersecting the magnetic equator. Dotted circular arcs are drawn at 1000 and 2000 km altitud

BEST AVAILABLE COPY

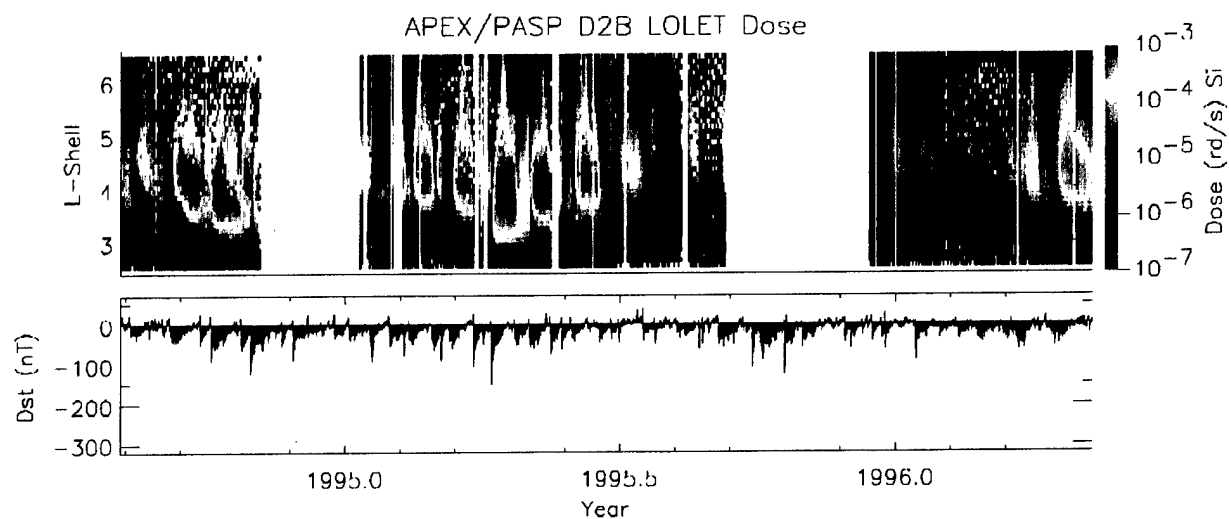


Fig. 4a. Plotted is the APEX mission survey. The top panel plots PASP dose rate (rd/s) in silicon (color coded) as a function of L (implicit B/B_0 dependence) and year. The bottom panel plots the magnetic activity index Dst (nT) as a function of year.

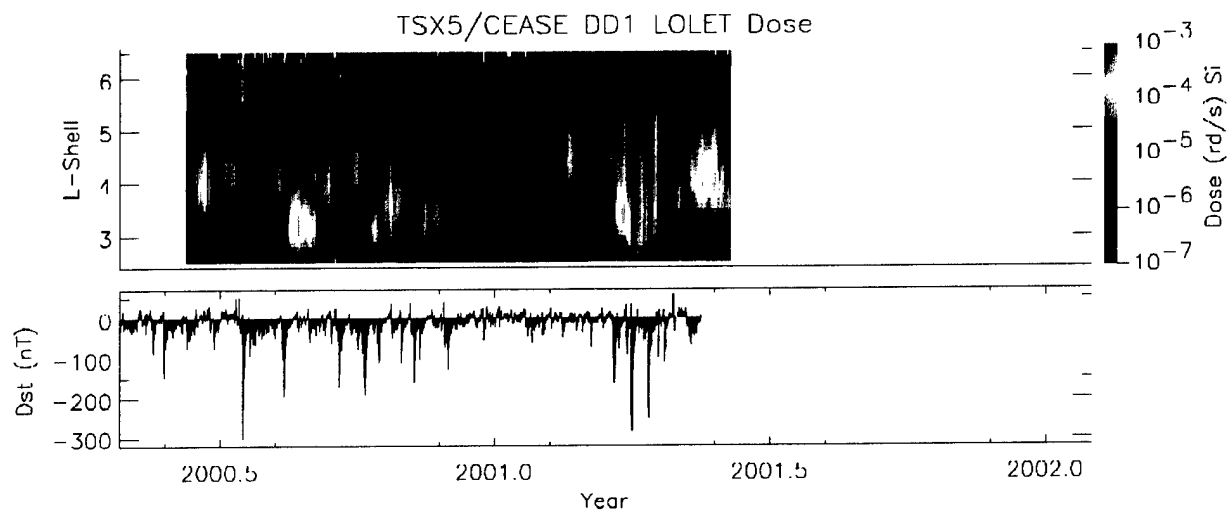


Fig. 4b. Plotted is the TSX5 mission survey. The top panel plots CEASE dose rate (rd/s) in silicon (color coded) as a function of L (implicit B/B_0 dependence) and year. The bottom panel plots the magnetic activity index Dst (nT) as a function of year. The length of the time scale is the same as that for Fig. 4a to facilitate comparison of temporal variations.

BEST AVAILABLE COPY

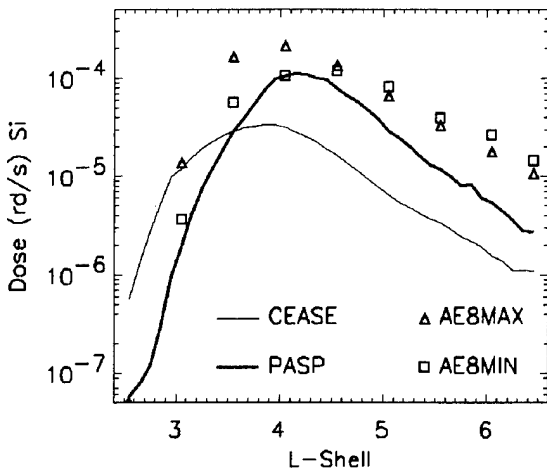


Fig. 5. APEX/PASP (heavy line) and TSX5/CEASE (thin line) mission average dose rates (rd/s) in silicon as a function of L (implicit B/B₀ dependence). Predicted dose rates from AE8MIN (squares) and AE8MAX (triangles) are included for comparison.

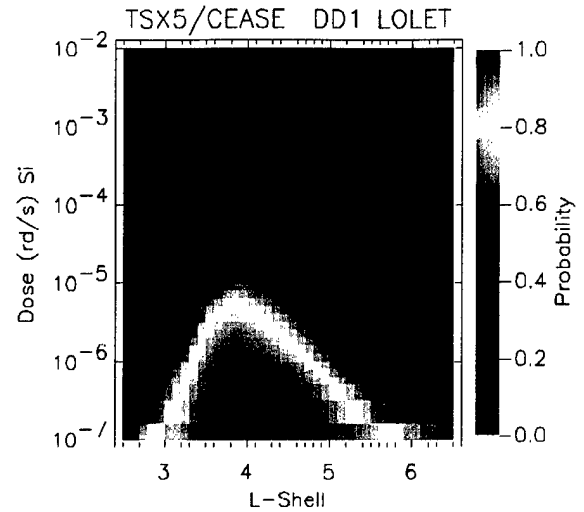


Fig. 6b. CEASE (solar minimum epoch) probabilistic dose model. Probability (color coded) for exceeding a threshold dose rate (rd/s in silicon) plotted as a function of dose threshold and L.

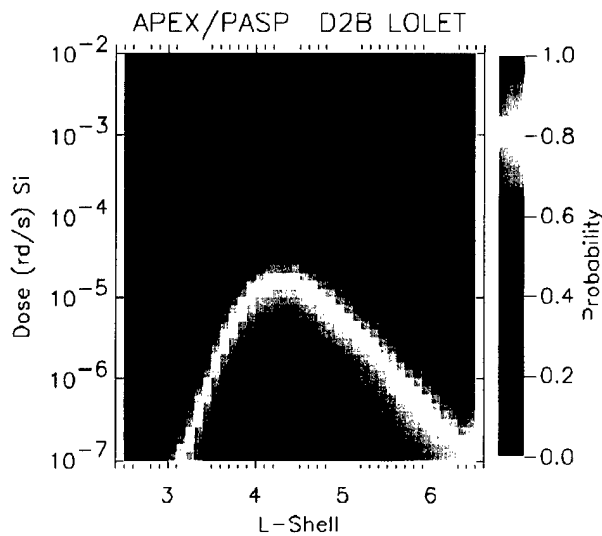


Fig. 6a. PASP (solar minimum epoch) probabilistic dose model. Probability (color coded) for exceeding a some threshold dose rate (rd/s in silicon) plotted as a function of dose threshold and L.

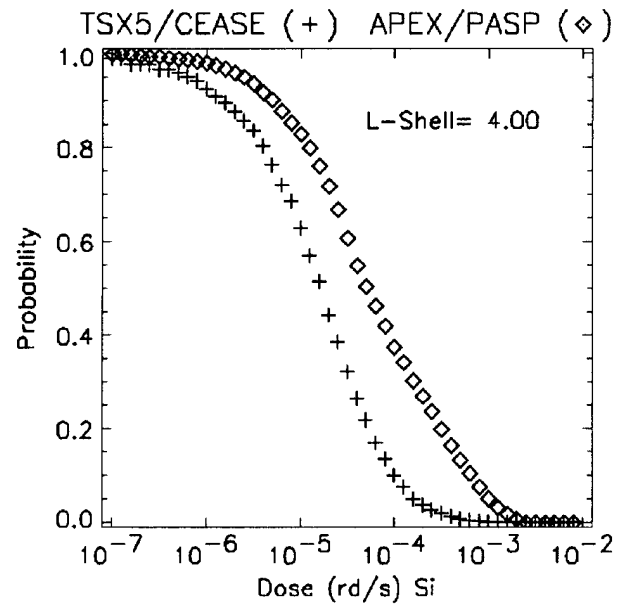


Fig. 7. This plot is a 2-D representation of the information in Fig. 6a and 6b for L=4.0. It gives the probability that the PASP (triangle) and CEASE (cross) dose rate at L=4 exceeds some specified threshold level (independent variable).

BEST AVAILABLE COPY

Appendix B

The paper by Dichter and Woolf [2003] that comprises Appendix B presents results of the Monte Carlo electron transport simulations that are summarized in Section 3.3 of this report.

Grazing Angle Proton Scattering: Effects on Chandra and XMM-Newton X-Ray Telescopes

Bronislaw K. Dichter and Stanley Woolf *Member, IEEE*

Abstract—A proton scattering process resulted in damage to one of the Chandra X-Ray telescope's focal plane detectors. In this process, incident protons were transmitted, by scattering off the telescope mirrors, to the focal plane. We identify the proton population responsible for the damage and, using a proper grazing angle formalism, we show that the standard calculations of grazing angle scattering will significantly under predict the expected proton flux at the focal plane.

I. INTRODUCTION

SEVERAL weeks into the Chandra X-Ray telescope mission, unexpected damage was observed to one of its cameras [1]. The problem was identified as radiation damage to the front illuminated charge coupled detectors (CCD) the Advanced CCD Imaging Spectrometer (ACIS). The amount of damage was orders of magnitude larger than was to be expected this early in the mission. This event resulted in intensive study of the transmission of protons through the Chandra and the European XMM-Newton x-ray telescopes [2] using the Monte Carlo computer code Geant4 [3]. Both of these instruments utilize grazing incidence mirrors to focus the x-rays onto the CCD cameras in the focal plane.

In this paper we will identify the particle population responsible for the damage and show that the transmission calculations of [2] use a model of proton scattering beyond its range of validity, leading to an underprediction of the transmission probability. We will present grazing angle scattering data and calculations and compare them to results computed using the same methods as are used in Geant4. Finally, we will discuss the effect that correct calculation of grazing angle scattering has on the calculated fluxes that reach the Chandra and XMM focal planes and suggest a way of obtaining more accurate results.

II. RADIATION DAMAGE TO CCD'S ON CHANDRA

Energy loss in Si solid state detectors, such as CCD's falls into two classes ionizing and non-ionizing energy loss

(NIEL). Ionizing energy loss is due to the distant collisions of the incident particles with the conduction band electrons in the target material. This type of process leads to temporary damage that can be reversed with time or by annealing the material. The NIEL process consists of collisions with the nuclei in the material lattice. Any such collision that results in the energy transfer greater than about 30 eV will knock the target atom from its location in the lattice. The result of this collision, one atom in an interstitial location and one vacancy in the lattice, is called a Frankel defect and is the most common type of bulk damage. Frankel defects act as charge carrier traps, removing electrons from the charge collection process. Protons with energy above a few keV have sufficient energy to cause this defect. The probability of causing the defect increases with energy up to about 100 keV and then decreases with increasing energy with an energy dependence of $1/E$ [4].

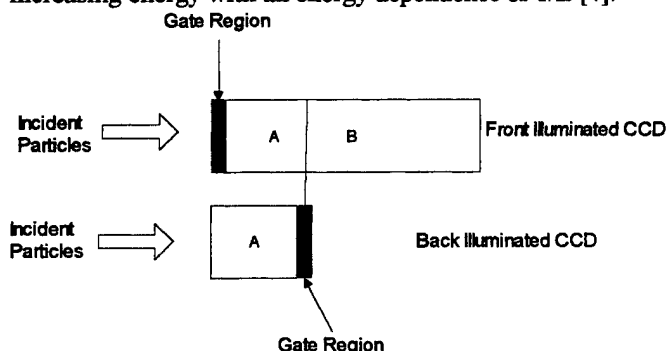


Fig 1. Configuration of the front and back illuminated CCD's in the Chandra instrument focal plane. Region A corresponds to the first 45 μm of Si facing the incident particles. Back illuminated device gate region is shielded from transmitted protons by the upstream region A. Front illuminated devices do not have such shielding.

The ACIS configuration of its 10 CCD's is shown in Fig. 1. Eight of the CCD's are front illuminated (FI), with the charge transfer gate region directly exposed to incident particles transmitted through the grazing optics of the telescope. Two are back illuminated (BI) and have the body of the device shielding the gate region. ACIS operates with a thin Polyamide film, with a light blocking aluminum coating upstream of the CCD's. The total mass density of the film and aluminum is sufficient to stop protons with $E < 80$ keV. During the first few weeks of the mission, the FI CCD's suffered a degradation of performance. The measure

Manuscript received 21 July 2002. This work was supported in part by the U.S. Air Force under Contract No. F19628-99-C-0077.

B. K Dichter is with the Air Force Research Laboratory, Space Weather Center, Hanscom AFB, MA 01731 USA (telephone: 781-377-3991)

S. Woolf is with the Arcon Corp. 260 Bear Hill Road, Waltham MA, 02154 USA (telephone: 781-890-3330, e-mail: stan@arcon.com).

of the small inefficiency in transferring electrons from one pixel to another during the readout cycles, or charge transfer inefficiency (CTI), was increasing far more rapidly than expected for the FI CCD's. The CTI for the

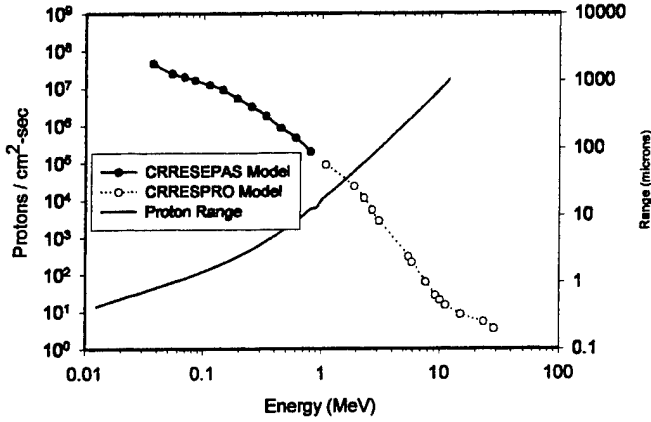


Fig 2. Integral proton fluence and range in Si plotted as a function of energy. Protons models are described in [5].

BI CCD's remained unchanged. The ACIS CCD integral proton fluence computed for the Chandra orbit is shown in Fig. 2. Our calculations assume that the incident proton population has an access path to the CCD's that does not degrade its spectral shape. We will justify this in Section 4. Electron fluences are not a concern because the low energy electrons ($E < 100$ keV) are swept away by the ACIS broom magnets and the higher energy electrons are both far less numerous and are highly inefficient producers of Frankel defects. The FI CCD's can be divided into Region A, the same length as BI CCD's, and remainder, Region B. Both BI and FI region A are sensitive to flux $f_A = 1.65 \times 10^7$ protons/cm²-s corresponding to $E > 80$ keV. The region B, however is only sensitive to $f_B = 2.37 \times 10^4$ protons/cm²-s corresponding to $E > 1,900$ keV. Since the ratio $f_B/f_A = 1.4 \times 10^{-3}$, the damage to the bulk silicon in region B is small compared to region A and can be neglected. Taking into account the fact the BI CCD's did not suffer any degradation it is likely that the damage occurred near the front of the devices. This is made more evident by computing $\langle R \rangle$, the average range of protons in Si, weighted by the incident particle flux $f(E)$,

$$\langle R \rangle = \frac{\int R(E) f(E) dE}{\int f(E) dE} \quad (1)$$

where $R(E)$ is the proton range [6]. The computed value is $\langle R \rangle = 4.8 \mu\text{m}$ and most of the incident protons will stop within $4.8 \mu\text{m}$ of surface, in or near the highly sensitive gate region. This distance corresponds to the range of a 300 keV proton, thus all protons with $E < 300$ keV will deposit their full energy in the gate region, protons with $E = 400$ keV will deposit 315 keV and the much less numerous 2 MeV

protons, 130 keV. Thus, if the external protons have access to the CCD's, the bulk of the damage will occur in the first few microns. This is verified by the work of one group [7] that has directly linked CTI increase to damage to the buried channel component of the CCD, located a fraction of a micron beneath the gate region.

We have shown that if the external protons have direct access to the CCD's, the population with energies in the range of 100-500 keV is responsible for the damage of the FI CCD's. In the next section will show how the proton transmission from outside the spacecraft to the CCD's takes place.

III. STANDARD CALCULATIONAL METHODS

The XMM team has used the Monte Carlo code Geant4 to calculate the proton transmission probability. We have chosen to use to use another well-established Monte Carlo code, MCNPX [8] to treat energetic proton scattering. Both Geant4 and MCNPX use condensed collision physics to compute the energy loss and angular scattering of a particle by considering the incident proton's collisions with atomic electrons and with atomic nuclei. Geant4 uses a "mixed" multiple scattering algorithm [3] to predict proton energy loss and scattering angle, while the MCNPX physics for determination of angular deflections is based on Rossi's Gaussian model [9], and in the energy range of interest here, a continuous-slowing-down energy loss model. In both Geant4 and MCNPX models, more numerous collisions with electrons result in small angular scattering and a small energy loss per collision. Less frequent collisions with target nuclei result in comparatively large scattering angles and energy losses. Each collision in this approach is considered to be independent of the others and it is the sum of all the small, random changes in angle and energy that accounts for the final incident particle scattering angle and degraded energy.

These procedures, and their underlying physics models, were initially developed for thin foil and bulk material scattering of protons and alpha particles [10]. While these scattering models are valid for moderately large angles of incidence, or cases where the incident particle is traveling in the bulk material, the fundamental assumption of independence of the collisions is not valid for grazing angles of incidence. In addition, the assumption that the incident particle will enter into the bulk material, if the particle trajectory is not exactly parallel with respect to the surface, is also not valid. In the next section we will present a conceptually correct way to handle grazing incidence beam-target interactions.

IV. GRAZING ANGLE SCATTERING

A. Energy Loss

In the past decade, grazing angle angular specular and near specular scattering has been studied as a means of deducing

the properties of the scattering surface. Song and Wang [11] computed trajectories of grazing incidence protons incident on a carbon surface. Their work showed that, in general, the incident particles traveled only through the electron plasma cloud outside the surface before being reflected (no collisions with atomic nuclei). Furthermore, the lengths of trajectories inside the plasma cloud were only weakly dependent on the energy and angle of incidence. This result provides an explanation for the experimental results obtained by Winter *et al.* [12] and Pfanzennder and Stolzle [13] that the most probable energy loss for a wide range of energies $30 < E < 710$ keV is of the order of 3 keV and does not depend on the angle of incidence. In addition, the energy spectra of the reflected protons are dominated by a Gaussian peak, centered on the most probable energy loss, with only small probabilities for greater energy losses.

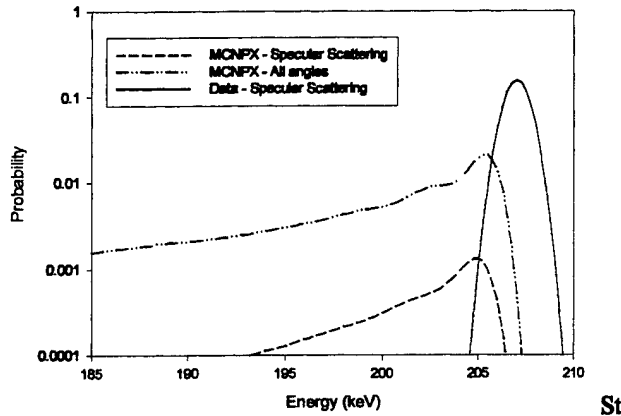


Fig. 3. Energy distributions of scattered 210 keV protons (aluminum target). Data curve is extracted from Winter *et al.* [12]. Specular scattering is for angle of incidence of 0.5° . "All angles" is for scattering between 0° and 90° .

Standard approach to scattering calculations cannot reproduce the effect of grazing angle trajectories that are reflected before striking the surface material. The differences between the two approaches are evident in Fig. 3. In this figure, the measured energy spectrum of 210 keV protons scattered off aluminum [12] is shown along with the results from an MCNPX calculation. As expected the MCNPX results have broad, low energy tail from the numerous high energy loss collisions with the atomic nuclei in the target material. A comparison of calculated and measured energy losses for protons incident on aluminum as a function of incident energy is shown in Fig. 4. The MCNPX calculated values show a much larger energy losses than the data. The agreement is even worse when the measured most probable values, which are very nearly average values, are compared to MCNPX average values. The effect of using the standard model of scattering when treating grazing angle scattering is the prediction of energy loss distributions that are highly asymmetric and very broad. This is true for MCNPX and the for the methods used in Geant4 [3]. The overall effect is for codes like MCNPX and Geant4 to predict larger energy losses than actually occur in the scattering process.

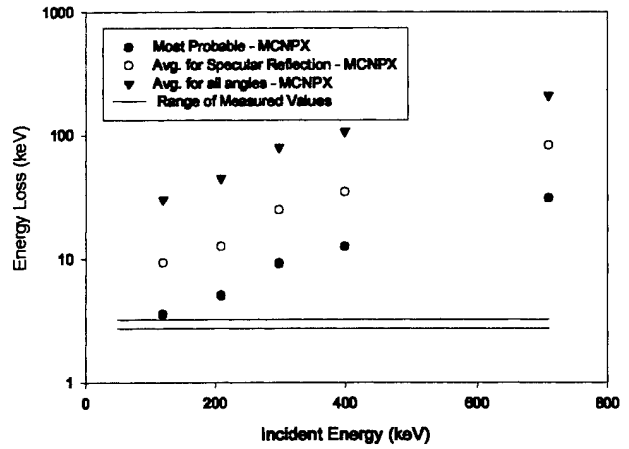


Fig. 4. Comparison of measured and computed energy loss of grazing incidence protons (aluminum target) as a function of incident energy. Measured most probable energy loss values [12] are all in the region between the two horizontal lines (all values were approximately 3 keV in the energy range of 50 to 710 keV). Due to the symmetry of the measured energy loss distributions [13], the measured most probable value is very close to the average value.

B. Angular Scattering

Angular scattering of the grazing incidence protons cannot be reproduced by the physics models used in Geant4 and MCNPX. These models assume that the proton does not react with the scattering surface until it enters and then is scattered as if it were traversing bulk material. In fact, the work of Song and Wang [11] shows the incident proton interacts with the surface long before it strikes it. In some cases the proton is reflected before it strikes the surface. For larger angles of incidence, the proton only enters the electron cloud that extends into the vacuum to a distance of a few nanometers out from the material surface. In general, for grazing angle scattering, the incident protons do not enter the bulk material at all.

The angular scattering of grazing angle incidence protons from a flat surface is dominated by a process with 1) an energy loss small compared to the incident energy and 2) angular scattering characterized by weak interaction with the electron plasma cloud. In this case the proper scattering response is that given by Firsov [14]

$$N(\psi, \theta) = \frac{3}{2\pi\psi} \frac{(\psi\theta)^{3/2}}{\psi^3 + \theta^3} \quad (2)$$

where N is the scattering response function, *i.e.* particle fraction per unit angle exiting the surface, ψ is the angle of incidence and θ is the scattering angle. Note that the results are independent of the properties of both the scattering medium and the incident particle. Firsov's formula was derived in the limit of zero scattering energy loss and is independent of the precise form of scattering law as long as

small angle scattering predominates. Both conditions are met in the case of grazing angle scattering. It is easy to show that the scattering function N peaks at $\psi = \theta$ (specular reflection) for all angles of incidence and that N is sharply peaked for small values of ψ and spreads out as ψ increases. Angular scattering curves, calculated both using MCNPX and (2), for two values of ψ are shown plotted in Fig. 5. Given that the vertical scale in Fig. 5 is logarithmic, it is evident, that the MCNPX distributions are much broader and have a much larger average scattering angle than the Firsov curves.

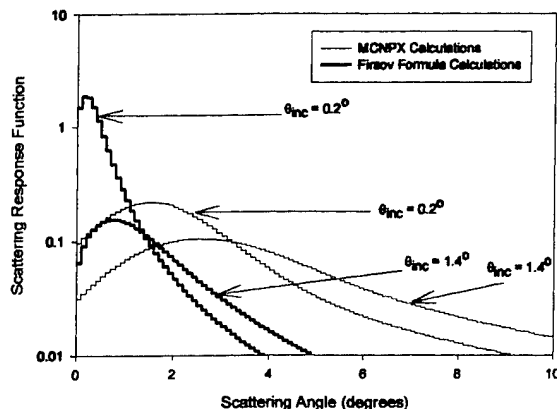


Fig. 5. Angular scattering distributions of 120 keV protons incident on aluminum calculated using MCNPX and Firsov distributions for two angles of incidence

The consequence of MCNPX predicted distributions being too broad and being centered on the wrong angles is that the computation of transmission through the telescope mirrors will lead to a too low result. In reality, grazing incidence protons undergo nearly specular reflection and, behaving very much like x-rays, are efficiently focused onto the CCD's in the focal plane. The MCNPX and Geant4 scattering calculations predict that the protons will be largely dispersed by the mirrors and will strike some other component of the telescope and be absorbed.

4. Conclusions

This paper has focused on scattering on aluminum rather than the mirror materials. This is due to the lack of availability of data for the mirror materials. However, the overall grazing scattering results depend only weakly on the scattering surface properties and will not change significantly for the mirror materials.

MCNPX and Geant4 calculations underestimate the effect of protons on focal plane instruments for two reasons:

- 1) The codes will overestimate the energy loss of protons, thus shifting to the spectrum of transmitted protons to a higher incident energy. This effectively reduces the calculated number of protons reaching the focal plane instruments since the

magnetospheric incident proton spectrum in falls off rapidly with energy.

and

- 2) The codes will calculate too large scattering angles thus directly decreasing the number of transmitted protons.

The ideal solution would to add the proper treatment of grazing angle scattering to the MCNPX and Geant4 codes. However, this may be a very major task and not easily accomplished. A good way of computing the upper limit of proton fluence in the focal plane is to assume that the protons undergo specular scattering with no energy loss, in effect they behave like photons. This approach will lead to only a slight overestimation of focal plane fluences

V. REFERENCES

- [1] Prigozhin G., Kissel S., Bautz M., Grant C., LaMarr B., Foster R., and Ricker G., "Characterization of the radiation damage in the Chandra X-ray CCDs", SPIE Proceedings Vol. 4140, pp.123-134, 2000.
- [2] R. Nartallo, E. Daly, H. Evans, P. Nieminen, F. Lei and P. Truscott, "Low-angle scattering of protons on the XMM-Newton optics and effects on the on-board CCD detectors", IEEE Trans. Nucl. Sci., vol. 48, pp.1815-1821, Dec 2001.
- [3] Geant4 Collaboration [Online]. Available: <http://wwwinfo.cern.ch/asd/geant4/geant4.html>
- [4] Dearnaley G., "Radiation damage by charged particles in silicon junction detectors", IEEE Trans. Nucl. Sci. Vol 10, pp 106-110, 1963
- [5] Hilmar, R. V., "AF-GeoSpace User's Manual, Air Force Research Laboratory AFRL-VS-TR-1999-1551.
- [6] Northcliffe L. C. and Schilling R. F., "Range and stopping-power tables for heavy ions," Nuclear Data Tables, Vol. A7, pp. 233-463, 1970.
- [7] Prigozhin G., Kissel S., Bautz M., Grant C., LaMarr B., Foster R., and Ricker G., "Correction of radiation damage in the Chandra X-ray CCDs," IEEE Workshop on Charge Coupled Devices and Advanced Image Sensing, Cal-Neva Resort, Nevada, June 2001.
- [8] MCNPX™, Version 2.1.5 User's Manual, L. S. Waters, Ed., Los Alamos Radiation Transport Group(X-6), November 14, 1999.
- [9] B. Rossi, "High Energy Particles", Prentice Hall, Inc., New York, 1965.
- [10] E. J. Williams, "Multiple scattering of fast electrons and alpha-particles, and 'curvature' of cloud tracks due to scattering", Physical Review, vol. 58, pp.292-306, August 1940.
- [11] Y-H. Song and Y-N Wang, "Numerical simulation for H⁺ ion-surface scattering under grazing incidence", NIM B153, pp. 186-190, 1999.
- [12] H. Winter, M. Wilke and M. Bergomaz, "Energy loss of fast protons in grazing scattering from an Al(111)-surface", NIM B125, pp.124-127, 1997.
- [13] R. Pfandzelter and F. Stolzle, "Probing the stopping power near the surface by specular reflection of protons from graphite", NIM B72, pp.163-175, 1992
- [14] O. B. Firsov, "Reflection of fast ions from a dense medium at glancing angles", Sov. Phys.- Doklady, vol. 11, No. 8, pp.732-733, 1967.